Chemical spectroscopy of individual human milk extracellular vesicles

DIPLOMA THESIS

submitted in partial fulfillment of the requirements for the degree of

Diplom-Ingenieur

in

Technical Chemistry

by

Nikolaus Hondl, BSc
Registration Number 01624304

to the Faculty of Technical Chemistry

at the TU Wien

Advisor: Prof. Bernhard Lendl

Assistance: Dr. Georg Ramer

Vienna, 29th September, 2022

Nikolaus Hondl

Bernhard Lendl

Die approbierte gedruckte Originalversion dieser Diplomarbeit ist an der TU Wien Bibliothek verfügbar
The approved original version of this thesis is available in print at TU Wien Bibliothek.
TU Bibliothek Your knowledge hub WIEN

Die approbierte gedruckte Originalversion dieser Diplomarbeit ist an der TU Wien Bibliothek verfügbar
The approved original version of this thesis is available in print at TU Wien Bibliothek.

Erklärung zur Verfassung der Arbeit

Nikolaus Hondl, BSc

Hiermit erkläre ich, dass ich diese Arbeit selbständig verfasst habe, dass ich die verwendeten Quellen und Hilfsmittel vollständig angegeben habe und dass ich die Stellen der Arbeit – einschließlich Tabellen, Karten und Abbildungen –, die anderen Werken oder dem Internet im Wortlaut oder dem Sinn nach entnommen sind, auf jeden Fall unter Angabe der Quelle als Entlehnung kenntlich gemacht habe.

Wien, 29. September 2022

Nikolaus Hondl

Die approbierte gedruckte Originalversion dieser Diplomarbeit ist an der TU Wien Bibliothek verfügbar
The approved original version of this thesis is available in print at TU Wien Bibliothek.
TU WIEN Bibliothek Your knowledge hub

Die approbierte gedruckte Originalversion dieser Diplomarbeit ist an der TU Wien Bibliothek verfügbar
The approved original version of this thesis is available in print at TU Wien Bibliothek.

Acknowledgements

First of all, I would like to thank Bernhard Lendl for the opportunity to write my Master's thesis in his group. Your commitment to science is a great source of inspiration.
I also want to thank my supervisor Georg. No matter what problems or questions I had, be it chemical or programming, you always went out of your way and found a solution for everything. Furthermore, I want to thank my colleagues in the research division Process Analytics for our pleasant conversations and our lunches together. I especially want to thank Ufuk for your always good-humoured manner and our joint training sessions in the morning. I also want to thank the Pincer boys, especially Julian, who introduced me to scientific work. Further, I would also like to thank all my student colleagues, especially Flora, who made sure that I passed all my exams. I want to thank all my friends I have made along the way, in particular the 'Bukowski-Group', with whom I had very interesting talks during the nights. And of course my two flatmates, Florian and Roland, thanks to whom I felt I played more FIFA than I studied. I also want to thank my family, especially my parents, Daniela and Norbert, for their unwavering support during my time as a student. Without you, this would not have been possible.
Finally, and most importantly, I want to thank my better half Doris. I am so happy and proud to have you in my life. You have always supported and motivated me through every obstacle. Without you I would be missing something. Thank you for everything!

Die approbierte gedruckte Originalversion dieser Diplomarbeit ist an der TU Wien Bibliothek verfügbar
The approved original version of this thesis is available in print at TU Wien Bibliothek.
TU WIEN Bibliothek Your knowledge hub

This diploma thesis has received funding from the COMET Center CHASE (project no. 868615), funded within the COMET Competence Centers for Excellent Technologies programme by the BMK, the BMDW, and the Federal Provinces of Upper Austria and Vienna. The COMET programme is managed by the Austrian Research Promotion Agency (FFG).

Die approbierte gedruckte Originalversion dieser Diplomarbeit ist an der TU Wien Bibliothek verfügbar
The approved original version of this thesis is available in print at TU Wien Bibliothek.
TU WIEN Bibliothek Your knowledge hub

Kurzfassung

Extrazelluläre Vesikel (EVs) sind nanoskalige Partikel, die mit verschiedenen physiologischen und pathologischen Funktionen in Verbindung gebracht werden. Sie spielen eine Schlüsselrolle bei der Kommunikation zwischen den Zellen und werden als Transportmittel für verschiedene Zellbestandteile verwendet. Es wird angenommen, dass EVs in der menschlichen Milch wichtig für die Ernährung von Säuglingen und für die Entwicklung ihrer erworbenen Immunität sind. Moderne Analysemethoden sind nicht in der Lage, markierungsfreie chemische Informationen auf der Ebene einzelner Vesikel zu liefern. Daher sind neue Analysetechniken erforderlich, um die chemischen Unterschiede innerhalb der EV-(Sub-)Population zu untersuchen [1]. Wir stellen ein Protokoll zur Erstellung von Profilen der Struktur und Zusammensetzung einzelner EVs mit Hilfe der photothermischen Rastersonden-Infrarotspektroskopie (AFM-IR) vor. Zunächst werden EVs mit Hilfe von mikrokontaktgedruckten Anti-CD9-Antikörpern auf einer Silikonoberfläche immobilisiert. AFM-IR liefert dann sowohl die EV-Größe als auch Spektren im mittleren Infrarotbereich für einzelne Vesikel. Die erhaltenen Spektren lassen sich gut mit Bulk-Referenzspektren vergleichen. Darüber hinaus liefern AFM-IR-Bilder spektrale Informationen für mehrere EVs innerhalb einer einzigen Messung. Das Stapeln von Bildern, die bei unterschiedlichen Wellenzahlen aufgenommen wurden, liefert hyperspektrale chemische Bilder von Vesikeln mit räumlicher Auflösung im Nanobereich.

Die approbierte gedruckte Originalversion dieser Diplomarbeit ist an der TU Wien Bibliothek verfügbar
The approved original version of this thesis is available in print at TU Wien Bibliothek.
TU Bibliothek Your knowledge hub WIEN

Die approbierte gedruckte Originalversion dieser Diplomarbeit ist an der TU Wien Bibliothek verfügbar
The approved original version of this thesis is available in print at TU Wien Bibliothek.

Abstract

Extracellular vesicles (EVs) are nanosized particles, which are associated with various physiological and pathological functions. They play a key role in intercell communication and are used as transport vehicles for various cell components. In human milk, EVs are believed to be important for the nutrition of infants and for the development of their acquired immunity. State of the art analysis methods are not able to provide label free chemical information at the single-vesicle level, hence new analysis techniques are required to study the chemical difference within EV (sub-)population [1]. We introduce a protocol to profile structure and composition of individual EVs with the help of photothermal scanning probe infrared spectroscopy (AFM-IR). First, EVs are immobilized onto a silicone surface using microcontact printed Anti-CD9 antibodies. AFM-IR then provides both EV size and mid-infrared spectra for individual vesicles. The received spectra compare favorably to bulk reference spectra. In addition, AFM-IR images provide spectral information for multiple EVs within a single measurement. Stacking images taken at different wavenumbers yields hyperspectral chemical images of vesicles at nanoscale spatial resolution.

Die approbierte gedruckte Originalversion dieser Diplomarbeit ist an der TU Wien Bibliothek verfügbar
The approved original version of this thesis is available in print at TU Wien Bibliothek.
TU WIEN Bibliothek Your knowledge hub

Die approbierte gedruckte Originalversion dieser Diplomarbeit ist an der TU Wien Bibliothek verfügbar
The approved original version of this thesis is available in print at TU Wien Bibliothek.

Contents

Kurzfassung **vii**

Abstract **ix**

Contents **xi**

1 Introduction **1**

1.1 Extracellular Vesicles 1

1.1.1 Extracellular Vesicles Isolation and Analysis 2

1.2 Infrared Spectroscopy 3

1.3 Atomic Force Microscopy 5

1.3.1 Principle of AFM 6

1.3.2 Contact Mode 6

1.3.3 Tapping Mode 7

1.4 Atomic Force Microscopy - Infrared Spectroscopy 9

1.4.1 AFM-IR Principle 9

1.5 Particle Isolation 10

1.5.1 Microcontact Printing 10

1.5.2 Antibody Binding 11

1.5.3 Diffusion in Particle Isolation 12

1.6 Aim of this Work 13

Die approbierte gedruckte Originalversion dieser Diplomarbeit ist an der TU Wien Bibliothek verfügbar
The approved original version of this thesis is available in print at TU Wien Bibliothek.
TU WIEN Bibliothek Your knowledge hub

2 Experimental **15**

2.1 Materials and Methods 15

2.1.1 Instruments 15

2.1.2 Chemicals 16

2.2 EV Capture Protocol 16

2.2.1 Cleaning of the Silicon Surface 17

2.2.2 Printing the Substrate 18

2.2.3 Incubation with Sample 20

2.2.4 Optimizing the Sample Incubation 21

2.3 First Vesicle 23

2.4 Processing of AFM-IR Images 26

2.4.1 Segmentation 27

2.4.2 Phase Cross Correlation 28

2.4.3 Linear Discriminant Analysis 29

2.4.4 Principal Component Analysis 30

2.4.5 Example Data Evaluation 31

Loading Data and Selecting Images 32

Correcting Image Drift 32

Stacking Images 33

Correction of height and phase images 33

Segmentation - Training Classifier 33

Segmentation - Classifier Prediction Probability 37

Segmentation - Watershed and Vesicle Extraction 38

Per-EV Evaluation 39

Vesicle Sizes 40

3 Results and Discussion **43**

Die approbierte gedruckte Originalversion dieser Diplomarbeit ist an der TU Wien Bibliothek verfügbar
The approved original version of this thesis is available in print at TU Wien Bibliothek.
TU Bibliothek Your knowledge hub WIEN

3.1 Dilution Adjustment 43
3.1.1 Direct Deposition without Incubation Chamber 43
3.1.2 Addition of Incubation Chamber 45
3.1.3 1:2 dilution 46
3.1.4 50:1 dilution 49
3.1.5 Adjusted Sample Dilution (1:10) 49
3.2 Structure and Chemical Composition of Individual EVs 53
3.2.1 AFM-IR Imaging 53
3.2.2 Data Analysis 56
Data Analysis of the Second Measurement 56
Data Analysis of the Third Measurement 62
3.3 Possible Sources of Error and Possibilities for Improvement 67

4 Conclusion **71**
4.1 Conclusion 71

List of Figures **73**

List of Tables **79**

List of Algorithms **81**

Bibliography **93**

Die approbierte gedruckte Originalversion dieser Diplomarbeit ist an der TU Wien Bibliothek verfügbar
The approved original version of this thesis is available in print at TU Wien Bibliothek.
TU WIEN Bibliothek Your knowledge hub

Die approbierte gedruckte Originalversion dieser Diplomarbeit ist an der TU Wien Bibliothek verfügbar
The approved original version of this thesis is available in print at TU Wien Bibliothek.

Die approbierte gedruckte Originalversion dieser Diplomarbeit ist an der TU Wien Bibliothek verfügbar
The approved original version of this thesis is available in print at TU Wien Bibliothek.

CHAPTER 1

Introduction

1.1 Extracellular Vesicles

Extracellular vesicles (EV) are membrane-enclosed, nano-sized vesicles, which range in size from 30 nm to 10.000 nm in diameter [2]. They are released by cells into the extracellular space and can be classified into three subtypes: exosomes, microvesicles (MVs) and apoptotic bodies. The classification is based on their biogenesis, release pathways, size, content and function [3]. Exosomes are formed by inwarding budding of the endosomal membrane and mature into multivesicular bodies during the process. These exosomes have a size ranging from 30 nm to 150 nm and are used as vehicles for various molecules, such as various proteins, mRNA, lipids [2, 3]. MVs are created through direct outward budding of the cell's plasma membrane and they have a size ranging from 100 nm to 1000 nm. They are used for the same purpose as exosomes [2, 3]. Apoptotic bodies are released by dying cells into the extracellular space and have a size from 50 nm to 5000 nm [3]. They are also used to transport materials to other cells [4]. EVs are released by various cell types and can be found in various biological fluids, such as breast milk, blood, urine, tears, amniotic fluid, lymph, gastric acid and bile [3, 5]. They were

first considered as garbage bags that get rid of nonfunctional cellular components, but are now recognized to take part in cell-to-cell communication, cell maintenance, coagulation, cellular homeostasis and inflammation. These functions depend on the ability of EVs to interact with recipient cells and deliver their contents. They can bind specific to targets via adhesion molecules. Exosomal tetraspanin complexes are used for targeting processes both *in vivo* and *in vitro* [5, 6].

Because of their ability to transport various cell material EVs have a great potential for an endogenous drug delivery system to the cells of interest [3]. They can also be exploited as biomarkers and can be used to diagnose or monitor a patient [3]. Therefore, EVs have a high potential as diagnostic markers for diseases such as breast and pancreatic cancer [7, 8] or Alzheimer's [9].

1.1.1 Extracellular Vesicles Isolation and Analysis

The next section gives an overview of the different ways to isolate and analyze EVs. For a more detailed explanation of each method, see Doyle et al. [3], Gurunathan et al. [5] and Willms et al. [2].

Isolation methods for EVs are based on isolation by size, immunoaffinity capture and precipitation. Ultracentrifugation techniques and size-based techniques, such as ultrafiltration and size exclusion chromatography (SEC), isolate EVs by size. Isolation by enzyme-linked immunosorbent assays (ELISA) relies on the use of antibodies to capture EVs. Methods like polyethylene glycol (PEG) precipitation or lectin induced agglutination are usually done using chemicals to precipitate the EVs. All these techniques result in a complex mixture of EVs and not in isolated single exosomes [3].

The analysis of EVs is separated into two types: physical analysis and chemical/compositional analysis. Physical analysis gives more insight into particle size or concentration and is performed via nanoparticle tracking analysis (NTA), dynamic light scattering (DLS), transmission electron microscopy (TEM) or scanning electron microscopy (SEM). NTA

Die approbierte gedruckte Originalversion dieser Diplomarbeit ist an der TU Wien Bibliothek verfügbar
The approved original version of this thesis is available in print at TU Wien Bibliothek.
TU Bibliothek Your knowledge hub WIEN

is able to determine both particle size and concentration, but it requires sample volumes of ~0.5 mL [10, 3]. However, with NTA it is also possible to get chemical information, if the exosomes are being labelled [11, 12]. With TEM and SEM it is possible to get the size distribution and morphology of EVs [3]. Chemical/biochemical/compositional analysis gives insight into the content of EV. Typically, immunodetection methods like flow cytometry, western blotting or proteomic analysis are used for this type of analysis [3]. Limitations of flow cytometry can be that the EVs are too small, since most of the current flow cytometers can only detect particles larger than 500 nm [13]. In western blotting, the vesicles need to be lysed and not intact anymore [14], thus western blotting is not able to analyze individual vesicles but only the bulk of a population. It is also possible to obtain information about EVs via IR spectroscopy [15], which will be discussed in the next section.

1.2 Infrared Spectroscopy

Infrared spectroscopy (IR) is a technique that probes molecular vibrations. It exploits the fact that molecules absorb radiation in the infrared spectral range at specific energies that correspond to the frequencies at which their vibrations happen. Mid-IR spectroscopy is non-destructive as well as non-contact and has the possibility to perform in situ and remote measurements [16]. IR can be divided into three regions, the far-IR ($< 400\,\mathrm{cm}^{-1}$), the mid-IR ($4000\,\mathrm{cm}^{-1}$ to $400\,\mathrm{cm}^{-1}$) and the near-IR ($13\,000\,\mathrm{cm}^{-1}$ to $4000\,\mathrm{cm}^{-1}$). Spectral features in the mid-IR typically correspond to fundamental molecular vibrations and are thus easy to interpret. The near-IR region consists of overtones or combinations of fundamental stretching bands in the mid-IR region. Far-IR contains information about heavy atoms or weak bonds such as hydrogen bonds [17, 18].

Each molecule has a limited number of fundamental vibrations. This number depends on its shape (straight or angled) and its number of atoms. As each atom has three spatial

Die approbierte gedruckte Originalversion dieser Diplomarbeit ist an der TU Wien Bibliothek verfügbar
The approved original version of this thesis is available in print at TU Wien Bibliothek.
TU Bibliothek Your knowledge hub WIEN

degrees of freedom (corresponding to position in three orthogonal dimensions in space), a molecule of N atoms has $3N$ degrees of freedom. Of those $3N$ degrees of freedom, three represent translational motion in mutually perpendicular directions (the x-, y- and z-axes), and three represent rotational motion about the x-, y- and z-axes, thus ending in $3N - 6$ degrees of freedom for non-linear molecules and $3N - 5$ for linear molecules [17]. These are all the ways the molecule can vibrate, however, not all of these vibrations are "active" in the infrared, i.e., the vibrational modes can be degenerated for molecules with a certain symmetry [19]. The properties of the molecule (mass and bond between atoms) also have an impact on frequencies of the vibration bands [20]. When the atoms are displaced from their equilibrium position, all atoms vibrate at a characteristic frequency, ν_i for each mode i [19]. Following Hooke's law, the vibrational energy states, $V_i v$, can be calculated using the following equation:

$$V_{iv} = h\nu_i \cdot (v_i + \frac{1}{2}) \tag{1.1}$$

Here, h is the Planck's constant, ν_i the fundamental frequency of one mode and v_i the vibrational quantum number. The fundamental frequency can be described by [20]:

$$f = \frac{1}{2\pi}\sqrt{\frac{k}{m_r}} \tag{1.2}$$

Where k is the spring constant and, assuming there are two atoms, m_r is the reduced mass $m_r = \frac{m_1 m_2}{m_1 + m_2}$. The frequency of a vibration thus depends on the type of the vibration (stretching, deformation,...), the strength of the bond between vibrating atoms and their mass, as seen in equation 1.2. Due to this dependence of the frequency on bond strength and atomic mass, it is possible to assign "group frequencies" vibrations of specific functional groups and use the mid-IR spectrum of a molecule to understand its

Die approbierte gedruckte Originalversion dieser Diplomarbeit ist an der TU Wien Bibliothek verfügbar
The approved original version of this thesis is available in print at TU Wien Bibliothek.
TU Bibliothek Your knowledge hub WIEN

structure. For example, from 4000 cm^{-1} to 2500 cm^{-1} are the vibrations of O-H, C-H and N-H stretching, whereas the region from 1500 cm^{-1} to 600 cm^{-1} shows all manner of bending vibrations [19].

IR spectroscopy was dramatically enhanced through the introduction of the fourier-transform (FT) principle, thus leading to FTIR. FTIR combines high-scanning speed and sensitivity with extended computer facilities for data manipulation and various accessories to its current state of productivity and versatility [16].

Another enhancement for mid-IR spectroscopy is the availability of quantum cascade lasers (QCLs). QCLs are made of thin semiconductor layers of varying materials, where electrons are injected into the upper state of the quantum well system until a electrical field is induced. The relaxation of the electrons in a lower intersubband generates mid-IR photons, with a energy of the difference between the two states. Wavelengths are determined by the thickness of the layers and allows tailoring of the emission wavelength over a wide range [21].

1.3 Atomic Force Microscopy

An atomic force microscope (AFM) is an instrument that allows to get surface topography of samples with sub-nanometer spatial resolution [22]. The high spatial resolution can scan samples in ultrahigh vacuum at cryogenic temperatures to see the jumps of individual atoms [23] or to observe biological reactions [24]. Besides that, nearly every sample can be measured, be it very hard samples such as ceramics or metallic nanoparticles or very soft samples such as flexible polymers, human cells or the DNA. Due to these properties, AFM is used in all fields of science [22].

Die approbierte gedruckte Originalversion dieser Diplomarbeit ist an der TU Wien Bibliothek verfügbar
The approved original version of this thesis is available in print at TU Wien Bibliothek.
TU Bibliothek Your knowledge hub WIEN

1.3.1 Principle of AFM

In contrast to conventional microscopes, AFM does not form an image by focusing light or electrons onto a sample. Instead, it mechanically probes the sample with a sharp probe mounted on a cantilever. As a result, the topography is available, as are certain characteristics such as height, length, width or volume can be identified. The signal is generated via an optical lever sensor system. A laser beam is reflected by the back side of the cantilever onto a position-sensitive photodetector. When the cantilever, in particular the sharp tip mounted on the cantilever, interacts with the sample, the cantilever is deflected. This leads to a change in the path of the reflected light which is sensed by the position-sensitive photodetector and allows to measure the tip sample force [22]. The two most commonly used AFM modes are contact mode (see section 1.3.2) and tapping mode (see section 1.3.3).

1.3.2 Contact Mode

The first mode developed for AFM was the contact mode. To understand the contact mode, force-distance curves are necessary, as shown in figure 1.1. The abscissa of a force-distance curve shows the distance the cantilever has been moved relative to the sample surface, while the ordinate shows the force [22].

As shown in figure 1.1 the force-distance curve has a hysteresis. When approaching the sample, the cantilever is considered to have zero deflection at the beginning until it is in contact with the sample (typically, attractive forces between tip and sample can also "grab" the tip slightly before it touches the sample - snap-in). As the tip continues to approach the sample, it applies an opposite force onto the tip. This is called the repulsive regime. Here, a combination of cantilever bending and sample compression happens, according to the properties of sample and tip. When the tip is retracted again, the force-distance curve initially follows the same trajectory as during the approach, just in

Die approbierte gedruckte Originalversion dieser Diplomarbeit ist an der TU Wien Bibliothek verfügbar
The approved original version of this thesis is available in print at TU Wien Bibliothek.
TU Bibliothek Your knowledge hub WIEN

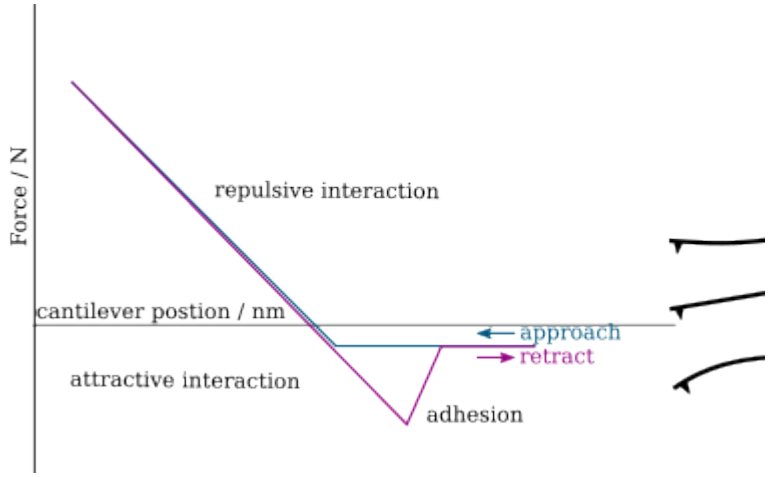

Figure 1.1: Simplified force-distance curve [20] showing the course of the tip during contact mode. On the right, the probe bending is illustrated.

the opposite direction. However, in the attractive regime, attractive forces between tip and sample will keep the tip at the surface even at distances where it was not in contact during the approach, until the tip finally tears away.

Contact mode AFM images are typically recorded in the repulsive as it allows more stable imaging (without hysteresis). A feedback system adjusts the vertical position of the cantilever to keep the deflection at a preset point, the set-point, and is thus able to image the topography through the provided height signal [22].

1.3.3 Tapping Mode

In tapping mode, the cantilever is made to oscillate near its resonant frequency so that the tip hits the sample on each oscillation. The energy associated with the oscillation has to be high enough to overcome the stickiness of the surface [25]. When the tip approaches the surface, the oscillation changes because of the interaction between the force field of the sample and the tip. Therefore, the amplitude and frequency of the cantilever changes, which can be measured by a force transducer or by the optical lever, and the topography image can be obtained [22].

Die approbierte gedruckte Originalversion dieser Diplomarbeit ist an der TU Wien Bibliothek verfügbar
The approved original version of this thesis is available in print at TU Wien Bibliothek.
TU Bibliothek Your knowledge hub WIEN

In tapping mode, a phase image can also be generated in addition to the topography image. The phase lag of the tip relative to the excitation signal is monitored and recorded, while the amplitude is kept at a set value. In the generated phase image additional information can be seen [26], like the softness of an extracellular vesicle.

In figure 1.2 the force-deflection curve can be seen. The tapping mode, or intermittent contact mode, oscillates through three regimes: the repulsive, attractive and non-interacting [22].

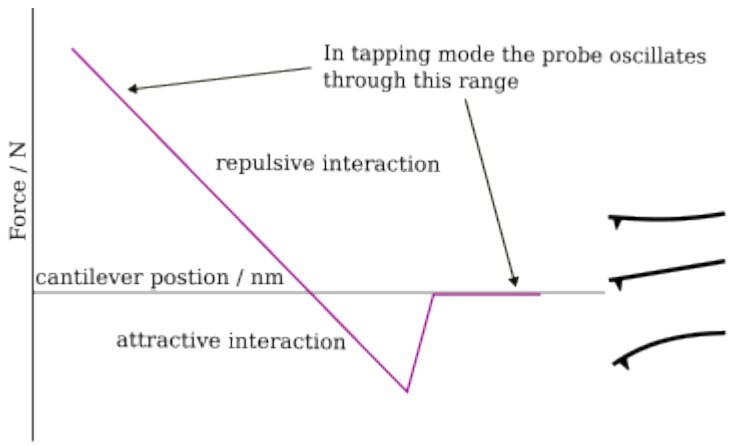

Figure 1.2: Operating regime of tapping mode [20]. The AFM probe oscillates back and forth between the repulsive and attractive regimes, losing contact completely in each cycle. On the right the bending of the cantilever is shown.

While one might assume that there is more potential for damage in this mode since the tip is hammering onto the sample, the opposite is the case. By adjusting the driving strength and the amplitude set point in tapping mode, the maximum tip sample force can be optimized/reduced. Due to intermittent contact in tapping mode, lateral forces are almost fully eliminated and the tip can break through the contamination layer on the sample, a layer of water and hydrocarbons, which can otherwise prevent the AFM to obtain clear images [22]. Therefore, in tapping mode the tip and the surface are not damaged and even soft samples can be measured [27].

Die approbierte gedruckte Originalversion dieser Diplomarbeit ist an der TU Wien Bibliothek verfügbar
The approved original version of this thesis is available in print at TU Wien Bibliothek.
TU Bibliothek Your knowledge hub WIEN

1.4 Atomic Force Microscopy - Infrared Spectroscopy

The two techniques, infrared spectroscopy and atomic force microscopy, described in sections 1.2 and 1.3 both have limitations. IR on the one hand is good to extract information about the chemical composition, but its spatial resolution is limited to several micrometers as a result of the Rayleigh criterion [28]. This relates to the minimal required distance (δ) between small point sources in a sample to distinguish them in an optical microscopy with the numerical aperture (NA) of the imaging system and the wavelength (λ) used for imaging:

$$\delta = 0.66\frac{\lambda}{NA} \tag{1.3}$$

AFM on the other hand provides good spatial resolution, but has no chemical sensitivity. To overcome these limitations, a combination of both techniques is used. By using the AFM tip to transduce the local photothermal sample expansion caused by the absorption of tunable laser pulses [29, 30], thus providing high spatial resolution ($\sim 20\,\mathrm{nm}$) [31, 32].

1.4.1 AFM-IR Principle

As mentioned in section 1.4 a tunable laser is focused on a desired region of the sample close to the AFM tip to cause local sample expansion. When the IR laser is set to a wavelength that is absorbed by the sample, the tip can be used to measure the absorbed radiation. IR absorption is directly measured by the thermal expansion resulting from the optical absorption. The thermal expansion increases as long as the light pulse lasts, and then the temperature of the sample decays back to normal, depending on the samples properties. Because of the thermal expansion, the cantilever experiences a force that drives it into oscillation, more specificly into multiple oscillatory modes (eigenmodes) over the course of short duration force impulses [33]. These eigenmodes can provide

Die approbierte gedruckte Originalversion dieser Diplomarbeit ist an der TU Wien Bibliothek verfügbar
The approved original version of this thesis is available in print at TU Wien Bibliothek.
TU Bibliothek Your knowledge hub WIEN

information about the stiffness of the sample, when operated in contact mode AFM [34]. In most cases, the oscillation amplitude of the cantilever is proportional to the amount of light absorbed and therefore directly proportional to the absorption coefficient. This oscillation amplitude can be measured at a fixed point as a function of the wavelength, which provides a signal directly proportional to the absorption coefficient. Consequently, it is possible to get IR absorption spectra that correlate to bulk transmission infrared spectroscopy. To obtain a chemical image, the measured oscillation amplitude can also be a function of the sample position [33]. AFM-IR has many applications including polymer characterization [35, 36], bacteria mapping [37], virus mapping [38] or semiconductors characterization [39].

1.5 Particle Isolation

1.5.1 Microcontact Printing

Microcontact printing (µCP) is a technique to print proteins or antibodies onto a surface [40, 41]. Its main function is the fabrication of well-defined 2D surface patterns on a desired sample [42]. In figure 1.3 it is shown how the principle of µCP works.

As a first step, a polydimethylsiloxane (PDMS) stamp with a pre-defined pattern is produced out of a silicon template master. After obtaining the stamp, it is soaked in a chemical or biological ink, for example, anti-CD9 antibodies for EVs [3]. Then the stamp is placed on the surface and some force is exerted to ensure that the desired pattern is printed on the substrate. In the last step, the stamp is removed and the desired pattern is printed on the substrate [42].

Die approbierte gedruckte Originalversion dieser Diplomarbeit ist an der TU Wien Bibliothek verfügbar
The approved original version of this thesis is available in print at TU Wien Bibliothek.
TU Bibliothek Your knowledge hub WIEN

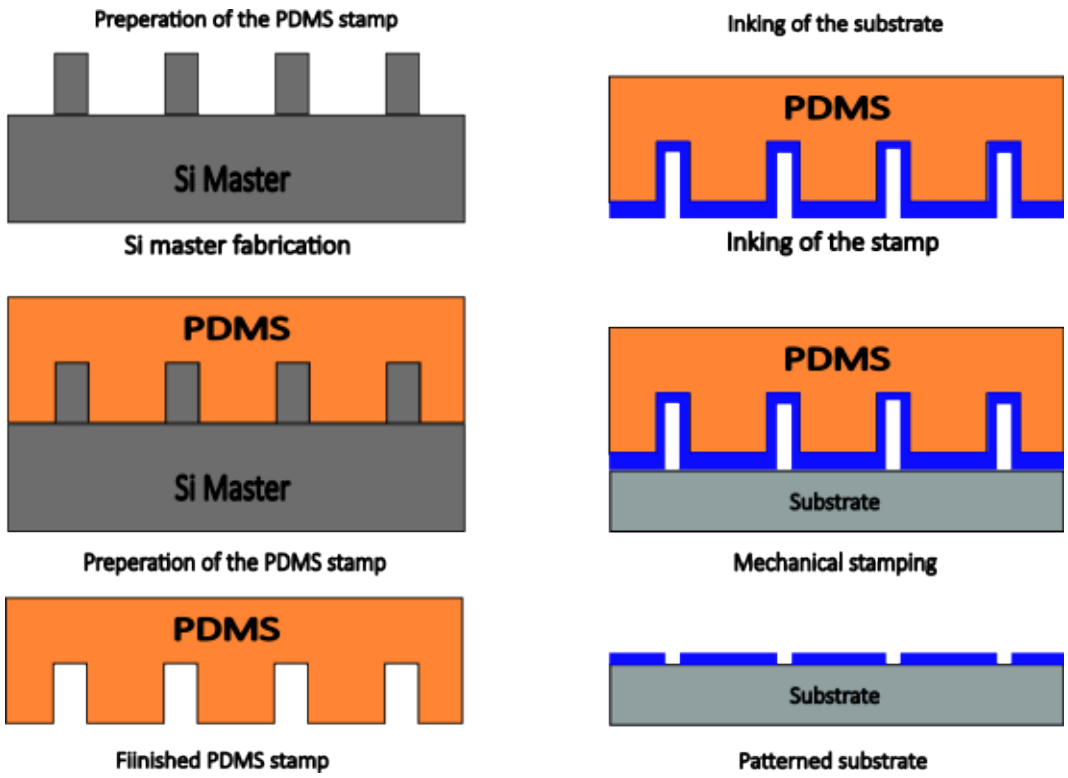

Figure 1.3: Principle of µCP

1.5.2 Antibody Binding

The antibodies, which are printed on a surface as described in section 1.5.1, have the important role to bind foreign molecules (antigens). Antigen-antibody interactions have a high specificity and affinity. The basic structure of an antibody contains two identical light chains and two heavy chains linked together via disulfide bonds. Five types of antibodies are known (IgG, IgA, IgM, IgD and IgE) and they distinguish in amino acid sequences as well as number of domains in heavy chains. Besides that, the light chains can also differ in two isotypes (λ and κ). The binding to an antigen happens through a lock-and-key mechanism as the antibody binds to the antigenic determinant (epitope) [43]. In figure 1.4, an antibody is depicted.

Die approbierte gedruckte Originalversion dieser Diplomarbeit ist an der TU Wien Bibliothek verfügbar
The approved original version of this thesis is available in print at TU Wien Bibliothek.
TU Bibliothek Your knowledge hub WIEN

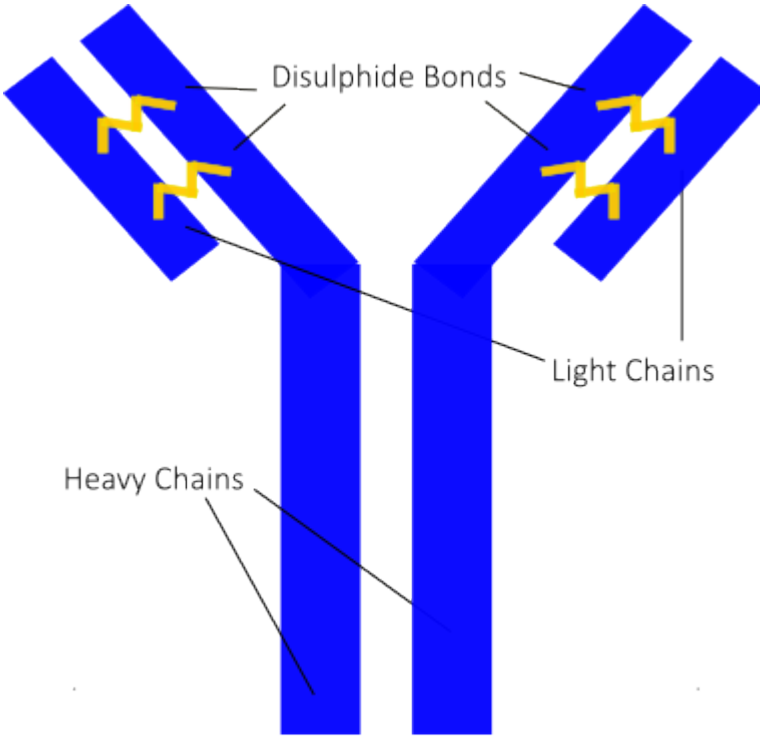

Figure 1.4: Schematic representation of a antibody

1.5.3 Diffusion in Particle Isolation

In particle isolation, the development normally focuses on the immobilization chemistry (see section 1.5.2) and the desired binding of the molecule onto the surface (see section 1.5.1). Besides these problems, it is also a challenge to transport the analytes, especially larger ones, to the surface [44], as they have larger diffusion coefficients. The equation to calculate the diffusion coefficient is depicted in equation 1.4 [44]. D is the diffusion coefficient in m/s^2, k_b is the Boltzmann constant in kJ/mol, T is the temperature in K, η the dynamic viscosity in mPa s of the liquid and R_0 the particle radius in m.

$$D = \frac{k_b \cdot T}{6 \cdot \pi \cdot \eta \cdot R_0} \tag{1.4}$$

With larger diffusion coefficients, the time a particle needs to get to the desired position

Die approbierte gedruckte Originalversion dieser Diplomarbeit ist an der TU Wien Bibliothek verfügbar
The approved original version of this thesis is available in print at TU Wien Bibliothek.
TU Bibliothek Your knowledge hub WIEN

increases. Equation 1.5 shows the equation to calculate the time, with t as time in s and D as diffusion coefficient in m/s^2.

$$t = \frac{x^2}{2 \cdot D} \tag{1.5}$$

A smart way to bypass this problem are either orbital shakers or microfluidic devices [44].

1.6 Aim of this Work

Analytical methods to analyze extracellular vesicles are already in use [3]. However, it is not yet possible to provide label-free chemical information at the single vesicle level. Due to this fact, the aim of this work is to provide a protocol, which fulfills exactly this task. To accomplish the given task, AnteoBind™ Biosensor, a chromium (III) metal complex in oligomeric form [45, 46], has been used to bind anti-CD9 antibodies on a silicon surface. Silicon was used for practical reasons as the AnteoBind™ Biosensor needs OH-groups to bond. The anti-CD9 antibodies on the other hand are able to bond with the CD9 antigens on the extracellular vesicles [3]. The steps to complete the given task were to optimize a protocol to capture the EVs, using microcontact printing. Afterwards, AFM-IR was used to analyze the EVs and to provide a method to determine the chemical composition.

Die approbierte gedruckte Originalversion dieser Diplomarbeit ist an der TU Wien Bibliothek verfügbar
The approved original version of this thesis is available in print at TU Wien Bibliothek.
TU Bibliothek Your knowledge hub WIEN

Die approbierte gedruckte Originalversion dieser Diplomarbeit ist an der TU Wien Bibliothek verfügbar
The approved original version of this thesis is available in print at TU Wien Bibliothek.

Die approbierte gedruckte Originalversion dieser Diplomarbeit ist an der TU Wien Bibliothek verfügbar
The approved original version of this thesis is available in print at TU Wien Bibliothek.
TU Bibliothek Your knowledge hub WIEN

CHAPTER 2

Experimental

The following chapter serves to explain the experimental procedures used to capture EVs on AFM-IR compatible substrates, the AFM-IR analysis and data processing performed to extract chemical composition and size information from AFM and AFM-IR images.

2.1 Materials and Methods

2.1.1 Instruments

AFM measurements were performed on a alpha 300 RSA+ (WITec, Ulm, Germany) confocal Raman and scanning probe system using 3XC-NN micro cantilevers (OPUS® by MikroMasch, Wetzlar, Germany). 3XC-NN combine three different cantilevers with different force constants and resonance frequencies. In this work the cantilever with a nominal a force constant of 9 N/m and a resonance frequency of 150 kHz was used.

AFM-IR measurements were performed using a Bruker nano-IR 3s coupled to a MIRcat-QT external cavity cascade laser array (EC-QCL) from Daylight Solutions. The measured spectra cover a range from 910 cm^{-1} to 1950 cm^{-1} and were obtained using tapping mode.

The cantilever was driven at its second resonance frequency (f2 = 1500 kHz) and the AFM-IR signal demodulated at the first resonance frequency (f1 = 250 kHz) with a digital lock-in amplifier (MFLI, Zurich Instruments). Cantilevers used were gold-coated and had a first free resonance at 300 kHz ± 100 kHz and a spring constant between 20 N m^{-1} and 75 N m^{-1} (Tap300GB-G from BudgetSensors). The laser source worked on a duty cycle up to 20 % and emitted laser pulses up to 500 mW. The laser power was adjusted between 14.75 % and 100 % of the original power with metal mesh attenuators. One to five spectra were recorded for each location. The whole instrument was purged with dry air generated by an adsorptive dry air generator.

2.1.2 Chemicals

All chemicals were used without further purification.

2-Propanole (C_3H_8O, *ROTH*, ROTISOLV®, ≥ 99.9%), AnteoBind™ Biosensor (*AnteoTech*), Anti-CD9 antibody produced in rabbit (*Sigma-Aldrich*, ~1 mg/mL, affinity isolated antibody, buffered aqueous solution), Bovine Serum Albumin (*Sigma-Aldrich*, heat shock fraction, protease and fatty acid free, pH 7, water soluble, ≥ 98%), Phosphate Buffered Saline tablet (*Sigma-Aldrich*, 1 tablet/200 mL water, 7.2 p to 7.6 pH), Silicon undoped and polished (*CrysTec*, thickness 0.525 mm, specific resistance > 3000 Ω cm Orientation (100)), ultra-pure water (*Milli-Q® Reference*, specific resistance 18.2 MΩ cm, TOC-value > 5 ppb)

2.2 EV Capture Protocol

The next subsections explain the preparation of the substrate, the cleaning, the coating with AnteoBind™ Biosensor to stamp antibodies onto it, backfilling of the pattern and incubation with the sample. The development of the capture protocol was necessary to overcome different challenges of this work. Analytes of the sample needed to be on the

Die approbierte gedruckte Originalversion dieser Diplomarbeit ist an der TU Wien Bibliothek verfügbar
The approved original version of this thesis is available in print at TU Wien Bibliothek.
TU Bibliothek Your knowledge hub WIEN

surface of the substrate and other components needed to be removed. Besides that, the sample concentration was rather low (10^8 particles/mL), so a way to get the analyte onto the surfaces had to be found.

2.2.1 Cleaning of the Silicon Surface

As the used AnteoBind™ Biosensor needs OH groups on the substrates for binding, silicon wafers had to be prepared to be plasma cleaned. The used high power expanded plasma cleaner from *Harrick Plasma* was operated at around 0.27 mbar and a radio frequency of 45 W. The residual gas, air, in the chamber of the plasma cleaner was ionized and the formed mixture of ions, free radicals, electrons and photons degraded the organic compounds, leaving OH groups at the surface. Figure 2.1 depicts the idea behind this step.

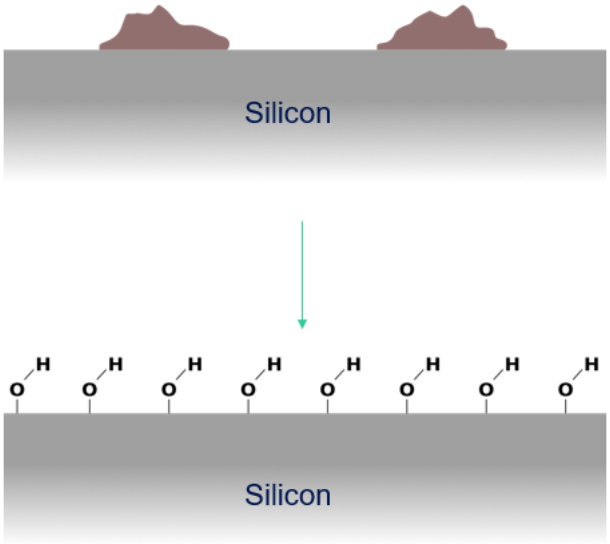

Figure 2.1: Plasma cleaning removes of organic compounds on the substrate and creates OH groups on the substrate.

The first step of the cleaning protocol was do wash the substrate with isopropanol for 10 min in the ultrasonic bath and repeat that step with ultra-pure water. Subsequently,

Die approbierte gedruckte Originalversion dieser Diplomarbeit ist an der TU Wien Bibliothek verfügbar
The approved original version of this thesis is available in print at TU Wien Bibliothek.
TU WIEN Bibliothek Your knowledge hub

the substrate was put into a plasma cleaner for 15 min. The plasma cleaner should remove all the organic impurities from the surface. To ensure that the surface was cleaned, it was also checked with the AFM.

2.2.2 Printing the Substrate

The cleaned substrate, treated as in chapter 2.2.1, was incubated with 100 µL of AnteoBind™ Biosensor for 45 min by just dropping the solution on, following Lindner et al. [41]. Afterwards, it was rinsed with ultra-pure water and dried under a stream of nitrogen to prevent the oxidation of the AnteoBind™ Biosensor. During the substrate incubation, the stamp for the microcontact printing was also incubated. Here, 30 µL of 20 µg/mL anti-CD9 antibodies were dropped onto the stamped and it was incubated for 15 min. Then it was rinsed with ultra-pure water and dried with nitrogen. The stamp was put onto the surface for one hour. In figure 2.2 the process is shown as a scheme.

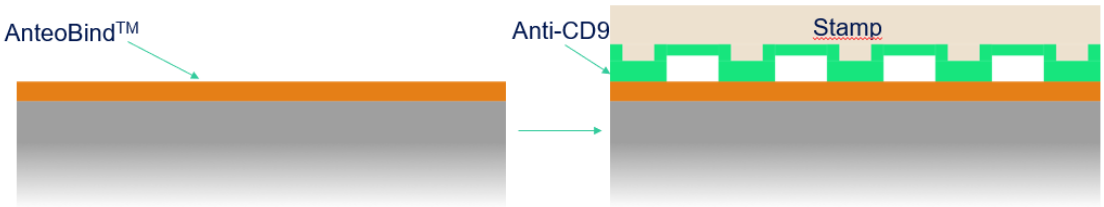

Figure 2.2: Scheme of the steps to µCP the silicon substrate

The pattern of the stamp, provided by the research area biophysics, was 3 µm circles spaced 3 µm apart in a 0.25 cm^2 squared area. In figure 2.3 the used stamp can be seen.

To check if the pattern on the stamp was printed on the substrate, an AFM image in tapping mode was obtained. The pattern had circles with a diameter of 3 µm, which are all 3 µm apart from each other. In figure 2.4 an image of the pattern can be seen.

The pattern is clearly visible and therefore the microcontact printing worked. Before the stamped silicon was ready for the incubation, the pattern had to be backfilled with

Die approbierte gedruckte Originalversion dieser Diplomarbeit ist an der TU Wien Bibliothek verfügbar
The approved original version of this thesis is available in print at TU Wien Bibliothek.
TU Bibliothek Your knowledge hub WIEN

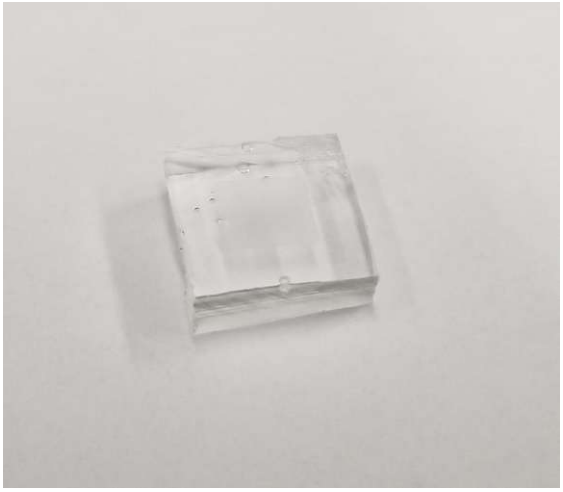

Figure 2.3: Used stamp for the microcontact printing.

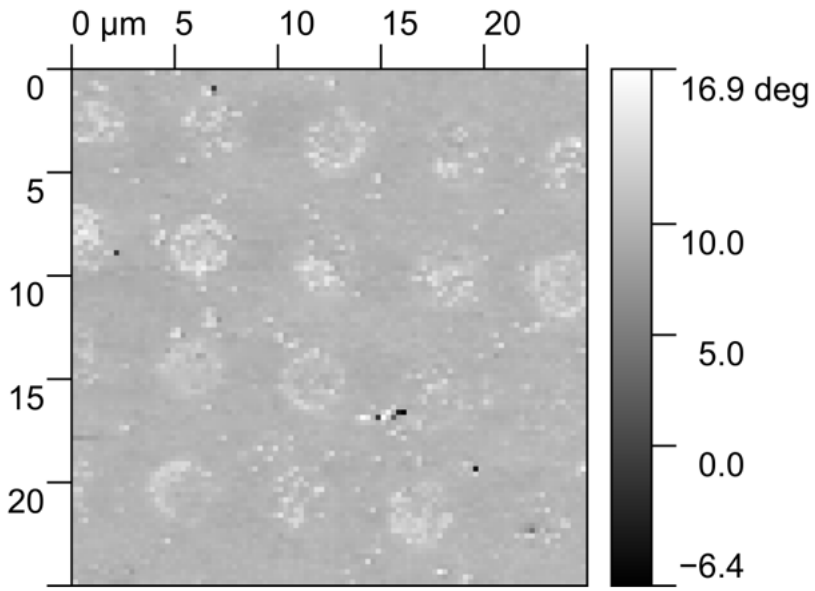

Figure 2.4: AFM phase image of the stamped pattern on the silicon surface

100 µL bovine serum albumin (BSA) in phosphate buffered saline (PBS) solution. This step was necessary to passivize the surface [41, 40] and to prevent analytes to be bound unspecific to the AnteoBind™ Biosensor in between the circles of the pattern. The BSA solution was just dripped on the stamped area and incubated for 15 min. Afterwards, it

Die approbierte gedruckte Originalversion dieser Diplomarbeit ist an der TU Wien Bibliothek verfügbar
The approved original version of this thesis is available in print at TU Wien Bibliothek.
TU Bibliothek Your knowledge hub WIEN

was washed away and dried with nitrogen. Figure 2.5 depicts the idea.

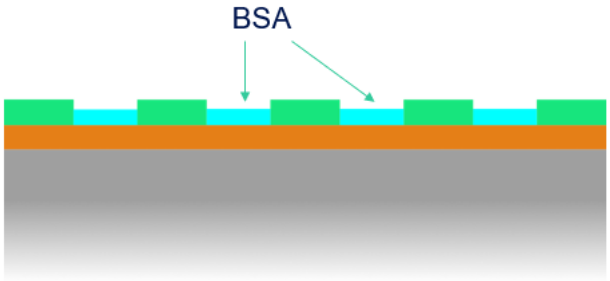

Figure 2.5: Backfilling the pattern with 100 µL BSA in PBS

2.2.3 Incubation with Sample

In the first iteration, the prepared silicon surface was incubated with 10 µL human milk exosome for one hour. The sample was flushed away with ultra-pure water and the silicon dried under a stream of nitrogen. In theory, the exosomes should be on the stamped parts of the surface, were they should be held by the anti-CD9 antibodies shown in figure (2.6).

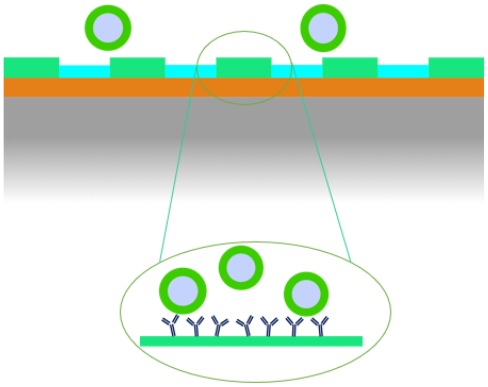

Figure 2.6: Anti-CD9 antibodies holding the exosomes from the human milk

An AFM image in tapping mode was made to see if any exosome could be found on the surface. Figure 2.7 shows the AFM image.

Die approbierte gedruckte Originalversion dieser Diplomarbeit ist an der TU Wien Bibliothek verfügbar
The approved original version of this thesis is available in print at TU Wien Bibliothek.
TU Bibliothek Your knowledge hub WIEN

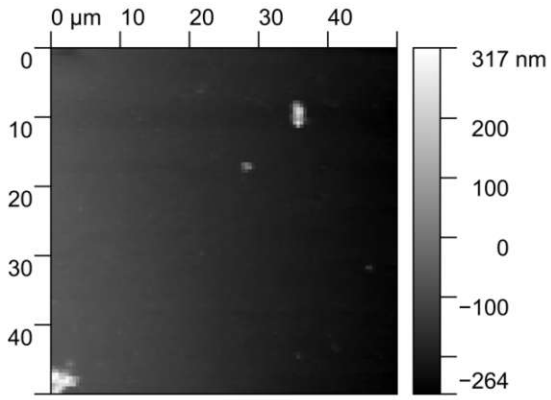

Figure 2.7: AFM image of the first incubated silicon with sample

The images show the surface of the silicon substrate. It shows no sign of any exosome from the sample. If any exosome would be there, they should be hold by the printed antibodies in a circle, but they are nowhere to be found. Two particles in the right half of the image can be seen, but these are too big, as one EV should have a diameter of 30 nm to 150 nm.

The consequence of this first iteration was that the low sample concentration and short incubation time could pose a problem and needs to be solved.

2.2.4 Optimizing the Sample Incubation

As described in section 1.5.3, besides immobilization and surface adhesion, the surface concentration of the analyte is also of importance. When using 10 µL of sample, the stamped pattern was covered, but the surface concentration of the analyte was low. Assuming an approximate vesicle concentration of 10^8 particles/mL, 10 µL of sample spread over the whole pattern would lead to a surface concentration of 1 EV per 25 μm^2. However, in this initial approach the area covered by the droplet could not be controlled as it increased with applied sample volume and depended on the wettability of the sample carrier. To decouple the covered surface area and allow a higher surface concentration FlexWell™ incubation chambers, as shown in figure 2.8, were used. These chambers stick

Die approbierte gedruckte Originalversion dieser Diplomarbeit ist an der TU Wien Bibliothek verfügbar
The approved original version of this thesis is available in print at TU Wien Bibliothek.
TU Bibliothek Your knowledge hub WIEN

to the substrate and allow to add a sample level up to 1 mm above the substrate without flowing off the carrier. This way 50 µL to 100 µL could be pippetted onto the sample at once.

To allow diffusion of vesicles across this large distance, longer incubation times were required, as explained in section 1.5.3. By using equation (1.4) and (1.5) and the following parameters, particle diameter of 80 nm, dynamic viscosity of 1.0087 mPa s [47] and a temperature of 298.15 K, we get a diffusion coefficient of $2.66 \times 10^{-12}\,\mathrm{m/s^2}$. A particle with that diffusion coefficient needs around 52 h to travel 1 mm.

Figure 2.8: Image of the used incubation chambers

Using incubation chambers, the incubation was repeated with a larger sample volume. After 52 hours, the incubated surface was washed with ultra-pure water and dried with a stream of nitrogen. Again, AFM imaging was used to search for exosomes on the surface. In figure 2.9 the image can be seen.

The diameter of the found particles in figure 2.9 matches the expected diameter of the exosomes. Besides that, they have been found on a circle of the printed pattern. Consequently, it can be assumed, that these particles have to be exosomes. To further identify them, an AFM-IR analysis was done, which is described in the next section 2.3.

Die approbierte gedruckte Originalversion dieser Diplomarbeit ist an der TU Wien Bibliothek verfügbar
The approved original version of this thesis is available in print at TU Wien Bibliothek.
TU Bibliothek Your knowledge hub WIEN

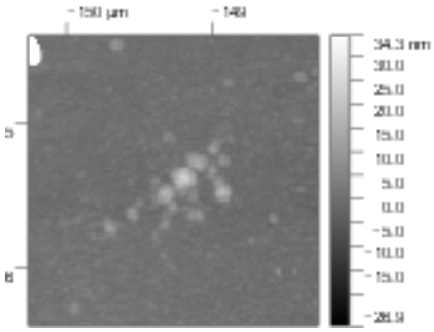

Figure 2.9: AFM image of EVs on the silicone substrate

2.3 First Vesicle

After confirming that something had been captured by the anti-CD9 antibodies, the first AFM-IR measurement was performed using tapping mode. At the start, the printed pattern was searched to find circles where EVs could have been captured. In figure 2.10, a phase image is shown.

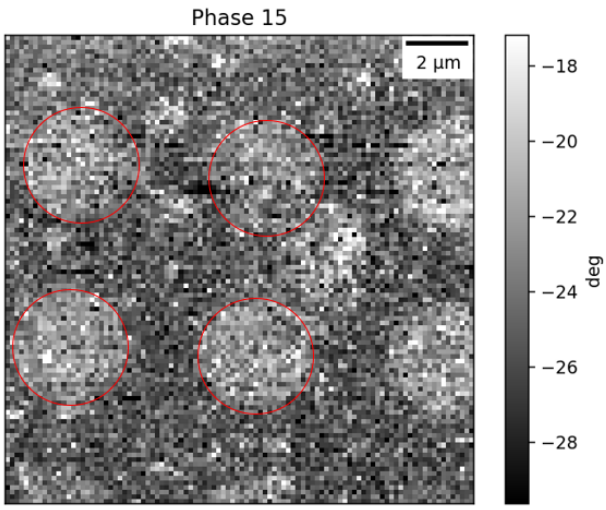

Figure 2.10: AFM-IR phase image of the first sample, with the visible stamped pattern (marked with red circles)

In the image, the printed pattern can be seen clearly. It shows again that the microcontact printing worked and that the pattern is still visible after the long incubation time. To

Die approbierte gedruckte Originalversion dieser Diplomarbeit ist an der TU Wien Bibliothek verfügbar
The approved original version of this thesis is available in print at TU Wien Bibliothek.
TU Bibliothek Your knowledge hub WIEN

now confirm that the found particles in section 2.2.4 are indeed exosomes, a circle from the images was chosen for closer examination. In figure 2.11, the phase and height image of this circle is shown.

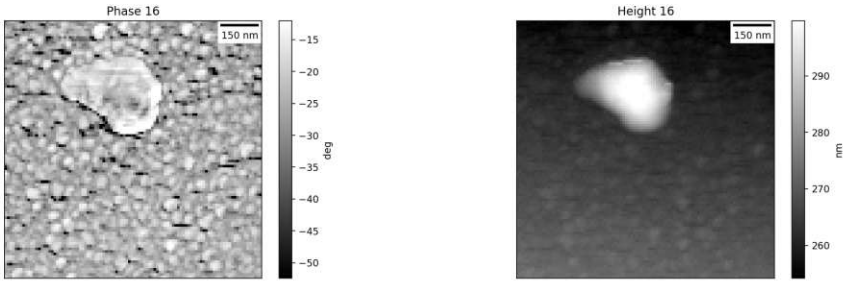

(a) Phase image of the focused circle (b) Height image of the focused circle

Figure 2.11: (a) phase image of the focused circle (b) height image of the focused circle

The depicted image shows a single suspected exosome. It is clearly visible in both the phase and height images. In addition, it corresponds to the diameter properties of exosomes, as it is assumed that the EVs are flattened by the incubation process [48]. Unfortunately, this is not a complete confirmation that this found particle is indeed an exosome. To confirm that, an EV spectra was acquired and compared to bulk data [15]. The bulk data was obtained by ultracentrifugation of human milk and dissolving it in PBS. A sample was then dried onto an ATR (Alpha II) and measured by it. In figure 2.12, the IR spectra are shown.

At first glance, the bulk data and the measured data are very comparable. Further discussion will take place in chapter 3. After finding this vesicle, it was also tested, if an AFM-IR images could be obtained. This was conducted by investigating the found wavenumbers in figure 2.12 and then carrying out the imaging. Here, a signal per pixel is obtained and matched into an image. In figure 2.13, the collected images can be seen.

It can be seen, that the imaging did not work sufficiently in the first iteration and that some problems occurred. These problems will also be discussed in chapter 3.

Die approbierte gedruckte Originalversion dieser Diplomarbeit ist an der TU Wien Bibliothek verfügbar
The approved original version of this thesis is available in print at TU Wien Bibliothek.
TU Bibliothek Your knowledge hub WIEN

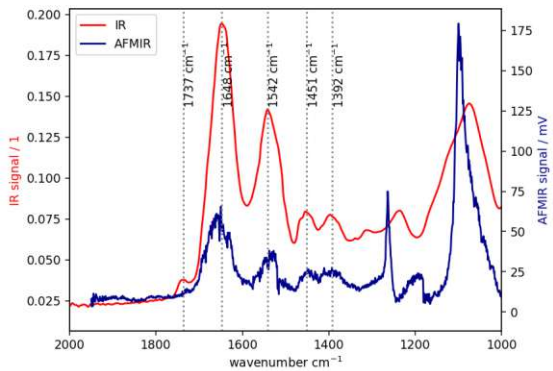

Figure 2.12: IR spectra comparison of the first found exosome. The bulk IR data (red line) matches the AFM-IR data (blue line) at the significant wavenumbers, see [15]

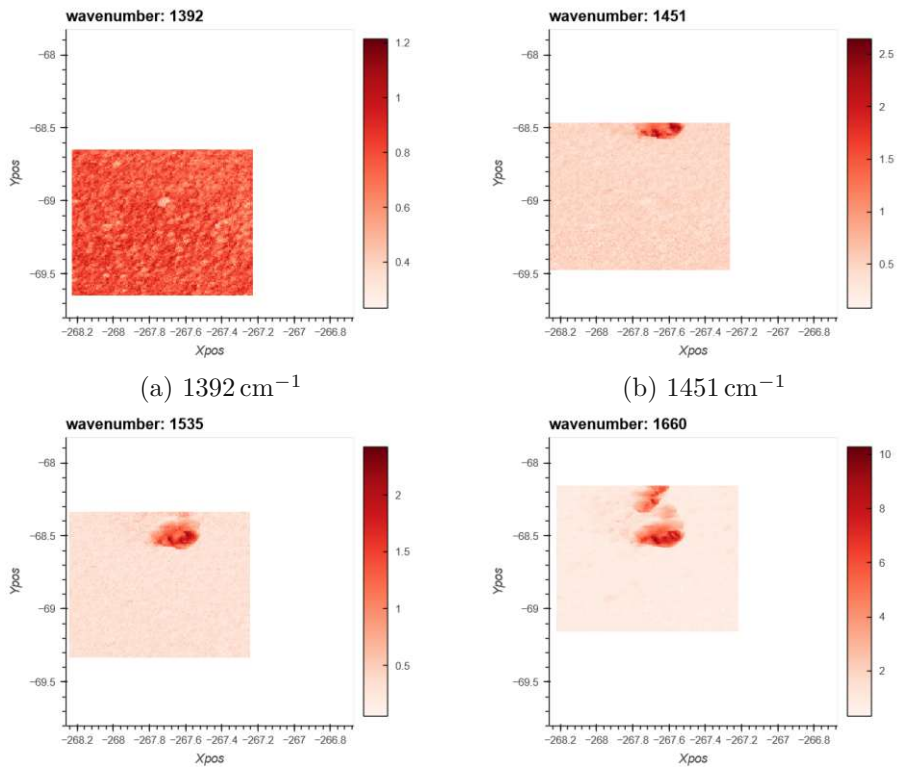

(a) $1392\,\mathrm{cm}^{-1}$ (b) $1451\,\mathrm{cm}^{-1}$

(c) $1535\,\mathrm{cm}^{-1}$ (d) $1660\,\mathrm{cm}^{-1}$

Figure 2.13: First iteration of the AFM-IR imaging with the respective wavenumbers (a) $1392\,\mathrm{cm}^{-1}$ (b) $1451\,\mathrm{cm}^{-1}$ (c) $1535\,\mathrm{cm}^{-1}$ and (d) $1660\,\mathrm{cm}^{-1}$

Die approbierte gedruckte Originalversion dieser Diplomarbeit ist an der TU Wien Bibliothek verfügbar
The approved original version of this thesis is available in print at TU Wien Bibliothek.
TU Bibliothek Your knowledge hub WIEN

2.4 Processing of AFM-IR Images

To retrieve the chemical composition of individual EVs from AFM-IR images, multiple single wavelength AFM-IR images had to be aligned to correct for lateral drift of the sample. Then, individual vesicles had to be found automatically from the topography and height images as well as collected together with the chemical data via image segmentation. To find common trends within the dataset, principal component analysis (PCA) was employed. Linear discriminant analysis (LDA) was used to prepare the data for the PCA. The following subsections explain these steps in more detail. The final part of this section shows the combined data evaluation of a typical dataset. In general, the data evaluation was done in Python with the help of various libraries, see table 2.1. Some of these libraries are for basic data visualization (matplotlib), but others use machine learning to perform linear discriminant analysis (LDA) or principal component analysis (PCA). The techniques, which are based on more complex algorithms, are explained in the following sections.

Die approbierte gedruckte Originalversion dieser Diplomarbeit ist an der TU Wien Bibliothek verfügbar
The approved original version of this thesis is available in print at TU Wien Bibliothek.
TU Bibliothek Your knowledge hub WIEN

Table 2.1: List of the various python libraries and their functions

Library	Version	Description
anasyspythontools	-	Library for reading nanoIR data files
matplotlib	3.1.3	Library to create static, animated, and interactive visualizations
numpy	1.22.4	Library to handle large, multi-dimensional arrays and matrices; it also contains many high-level mathematical functions to operate on the arrays
pandas	1.4.3	Library to analyze and manipulate large data; it offers a data structure, which is easy to handle with the built in functions, e.g. indexing, reshaping, slicing
scikit-image	0.19.3	Library for image processing; contains algorithms, which allow for segmentation, analysis, filtering, morphology, feature detection and so on
scikit-learn	1.1.1	Library that performs machine learning tasks; features algorithms for classification, regression and clustering
sklearn-xarray	0.4.0	Library that combines n-dimensional labeled arrays with machine learning tools of scikit-learn
xarray	2022.3.0	Library that handles labeled multi-dimensional arrays; features functions for advanced analytics and visualization

2.4.1 Segmentation

Image segmentation is the process of splitting an image into several smaller, meaningful regions. This segmentation was applied to find all individual vesicles from an AFM image. It was performed using functions from the scikit-image python package. The first part of this algorithm uses the Sobel-filter [49] to find edges in a image. After that, a pre-processed image or pre-processed data, where for example, a linear discriminant analysis was performed, is used to mark the foreground and the background. In the next step, the watershed algorithm [50] is used. The image gets separated into marked basins and these get filled until they meet another basin and form a wall [50]. Through this process, the image gets separated into different parts. In the last step, the found

Die approbierte gedruckte Originalversion dieser Diplomarbeit ist an der TU Wien Bibliothek verfügbar
The approved original version of this thesis is available in print at TU Wien Bibliothek.
TU Bibliothek Your knowledge hub WIEN

segments are enlarged, to increase visibility.

2.4.2 Phase Cross Correlation

Phase cross-correlation is a technique to find the relative shift between two images or signals. This is used to align them in a subsequent step. In layperson's terms, cross-correlation shifts one image against the other and determines at which shift they are most similar by multiplying all coinciding elements and then summing them over all these products. The shift at which the highest correlation is achieved, is the one at which the images are most similar. For large images, directly determining the cross-correlation is very inefficient as two images of $N \times N$ pixels would require N^2 shifts times N^2 multiplications. Instead, phase cross correlation [51] uses fast Fourier transform (denoted by $\mathcal{F}()$ to determine the cross correlation based on the following identity between correlation ($\star$) of functions and the product ($\cdot$) of their Fourier transform ($\overline{\square}$ denotes the conjugate):

$$\mathcal{F}(f \star g) = \overline{\mathcal{F}(f)} \cdot \mathcal{F}(g) \tag{2.1}$$

An example can be seen in figure 2.14, where two height images are aligned via PCC.

Die approbierte gedruckte Originalversion dieser Diplomarbeit ist an der TU Wien Bibliothek verfügbar
The approved original version of this thesis is available in print at TU Wien Bibliothek.
TU Bibliothek Your knowledge hub WIEN

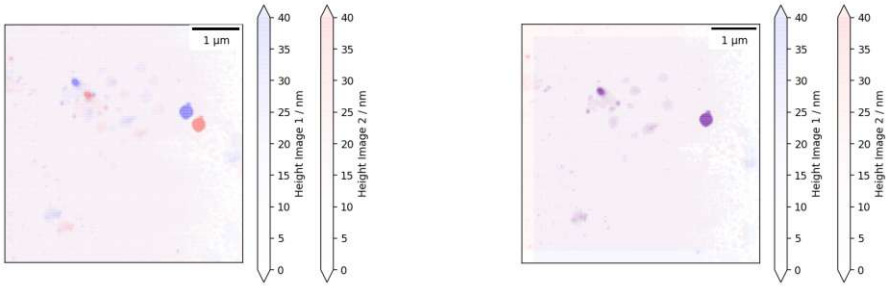

(a) Two height images before PCC

(b) Same height images aligned after the PCC

Figure 2.14: (a) Two height images with a clear deviation from each other (b) The same height images after PCC was carried out, thus they are aligned in the same way

2.4.3 Linear Discriminant Analysis

Linear discriminant analysis (LDA) is a supervised classification algorithm. Classification in machine learning is the task of assigning samples to groups, for example, in the case of this thesis, pixels in images can be assigned to the groups "EVs" and "non-EVs". A supervised algorithm requires training data where the input and the expected output (e.g. the expected class) is known to create a function which can predict the output for new inputs [52]. In layperson's terms, the algorithm finds a hyperplane that separates the two groups as well as possible. Figure 2.15 shows graphically how an LDA works. A term relating to LDA that will be required later is the so-called "decision function". For LDA, this decision function is the Mahalanobis distance [53] between each sample and the mean of instead of the classes. A sample is assigned to the class to which it has the lowest Mahalanobis [1] distance to.

[1] Mahalanobis distance is the Euclidian distance weighted by the variance of the class.

Die approbierte gedruckte Originalversion dieser Diplomarbeit ist an der TU Wien Bibliothek verfügbar
The approved original version of this thesis is available in print at TU Wien Bibliothek.
TU Bibliothek Your knowledge hub WIEN

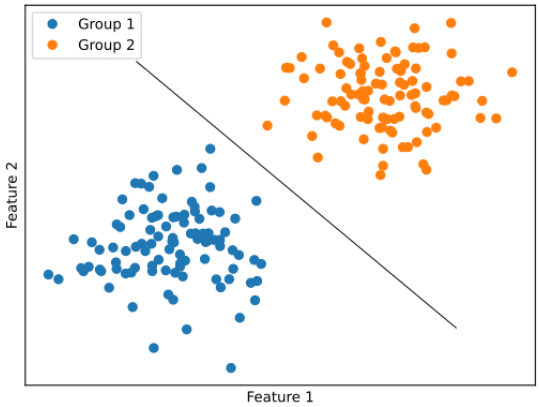

Figure 2.15: Two groups, with assigned features, which are being separated by the calculated hyperplane.

2.4.4 Principal Component Analysis

Principal component analysis (PCA) is an unsupervised machine learning algorithm (originally invented by Karl Pearson [54]). Unsupervised algorithms learn to find patterns in unmarked data [52]. Unmarked means that the data is not labelled and the algorithm is tasked with finding trends in the data itself. PCA finds orthogonal directions of the largest variance in the dataset - so-called principal components (PC) - and maps each sample onto these principal components [55]. PCs are a new coordinate system that might allow to represent the original dataset better. While a N dimensional dataset (i.e., a dataset with N variables) can have up to N principal components, higher PCs usually only describe noise in the dataset and account for low variance. Hence, by only using the first few PCs, the important information in a dataset can often be retained while the dimensionality can be reduced significantly. In figure 2.16, PCA is applied to a two-dimensional dataset to visualize its behavior. Most of the variance in this dataset lies in a direction that does not coincide with either axis of the coordinate system. PCA detects the major direction of variance (PC1) as well as a second principal component,

Die approbierte gedruckte Originalversion dieser Diplomarbeit ist an der TU Wien Bibliothek verfügbar
The approved original version of this thesis is available in print at TU Wien Bibliothek.
TU Bibliothek Your knowledge hub WIEN

orthogonal to PC1. The directions of PC1 and PC2 are drawn as lines in figure 2.16. Two important terms that are used when discussing the results of PCA are "scores" and "loadings". Scores are results of mapping samples onto principal components. Loadings describe the contribution of each variable to a principal component.

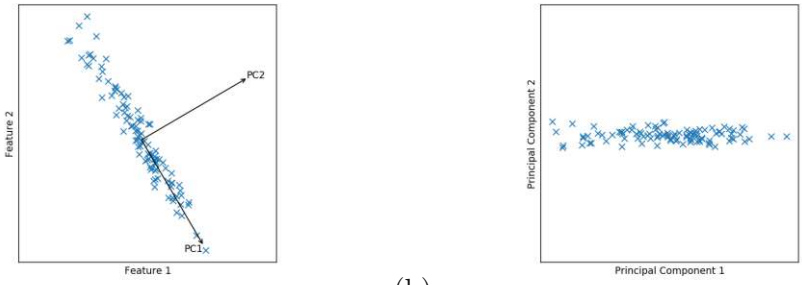

(a) (b)

Figure 2.16: (a) Two-dimensional dataset with two features visualized. Most of the variance lies in one direction (marked as PC1) and describes the majority of the data. The second principal component (marked as PC2) lies orthogonal to PC1. (b) PC score plot of the dataset with the principal components as axis. Useful for clustering of the data along the selected principal components.

2.4.5 Example Data Evaluation

Once a sample preparation method and measurement protocol had been established data from all AFM-IR imaging experiments were evaluated according to a similar scheme. Below the steps in this scheme are outlined. In the results and discussion chapter of this work, specific (hyper-)parameters and deviations from this scheme are pointed out, if required. The following steps were performed:

1. loading data and selecting images
2. correcting image drift
3. stacking images
4. correction of height and phase images

Die approbierte gedruckte Originalversion dieser Diplomarbeit ist an der TU Wien Bibliothek verfügbar
The approved original version of this thesis is available in print at TU Wien Bibliothek.
TU Bibliothek Your knowledge hub WIEN

5. segmentation - training classifier
6. segmentation - classifier prediction probability
7. segmentation - watershed and vesicle extraction
8. per-EV evaluation
9. vesicle sizes

Loading Data and Selecting Images A measurement file created on nanoIR instrument contains multiple images. When inserting a new sample, measurements are performed to find a good sample location and to optimize measurement parameters. These images are stored but are not used for further evaluation. Once all parameters are selected a set number of images at specified wavenumbers and laser powers are collected. Only this last series of images is used for evaluation. The first step in the evaluation is to open the data file in python and select the images for data evaluation. These images are then converted to `xarray.Dataset` types for easier handling. The code for this first step can be found in the appendix in listing 4.1.

Correcting Image Drift Due to various reasons (creep of the piezo, change of ambient temperature,...) successive AFM images are slightly shifted. To assemble meaningful hyperspectral images, this shift needs to be corrected first. This was achieved via PCC described in section 2.4.2. Before applying PCC, the topography image is preprocessed using the following function:

```
def nanquantile_correct(arr, dim="x"):
    return xr.apply_ufunc(
        lambda x: x - np.nanquantile(x, .01),
        arr,
        input_core_dims=[[dim]],
        output_core_dims=[[dim]],
```


Die approbierte gedruckte Originalversion dieser Diplomarbeit ist an der TU Wien Bibliothek verfügbar
The approved original version of this thesis is available in print at TU Wien Bibliothek.
TU Bibliothek Your knowledge hub WIEN

```
        vectorize=True)
```

In `nanquantile_correct` the 1% quantile is used instead of the minimum to be robust against outliers. The result of the PCC is stored in an attribute of the dataset.

Stacking Images To better handle the data, it was stacked into one dataset. Here, all the properties are saved as coordinates, for example 'wavenumber', which can be accessed individually. In addition, if the data is not complete after the shift, since not every image has all the pixels, these are filled with 'not a number' (NaN). This is shown in listing 4.2 in the appendix.

Correction of height and phase images After the first few steps, the data for the phase and height images have to undergo a correction. The code can be seen here 4.3. With these steps, it is already possible to display the data as images, for example, the height image of a sample in figure 2.17.

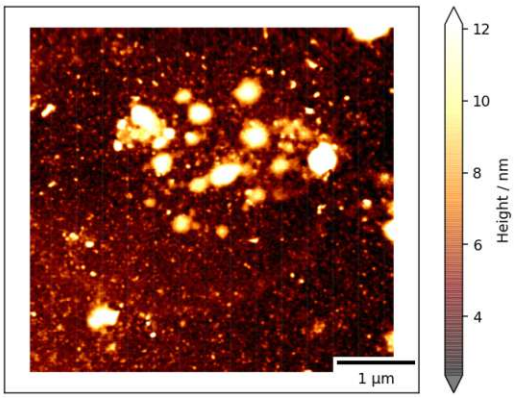

Figure 2.17: Height image after preprocessing, stacking and averaging

Segmentation - Training Classifier For image segmentation, first pixels that are likely to be recorded on a vesicle or on the substrate have to be identified. As vesicles

Die approbierte gedruckte Originalversion dieser Diplomarbeit ist an der TU Wien Bibliothek verfügbar
The approved original version of this thesis is available in print at TU Wien Bibliothek.
TU Bibliothek Your knowledge hub WIEN

are both higher and softer than the substrate, either the topography image or the phase image contains information about the "vesicleness" of a pixel. To allow for a more robust assignment, we combined topography and phase using LDA. First, training data has to be chosen that contains pixels known to be vesicles and pixels known to be substrates. This was done graphically: the user (author) uses the mouse to select a few areas known to be in either "EVs" or "non-EVs" class on top of a topography image (see code in listing 4.4). In figure 2.18, this is shown on an example image.

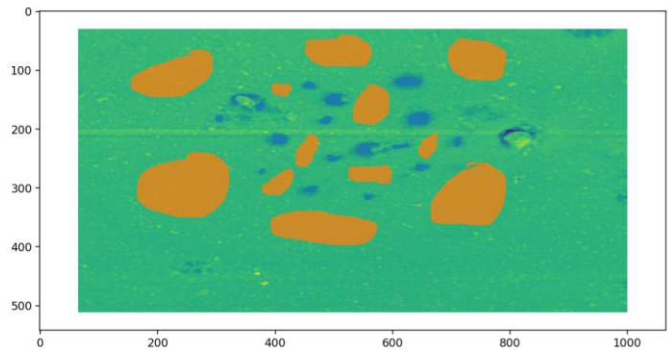

Figure 2.18: Identified areas on a topography image by the user, which are associated to "EVs" (blue) and "non-EVs" (orange). The chosen data is used as training data for the LDA.

Once the user had finished drawing the mask for the training dataset, all marked pixels were extracted into a `pandas.Dataframe` structure. Dataframes are two-dimensional tables with ordered columns and rows, which can be easily indexed and manipulated. An example is shown in table 2.2. Code for extracting data is shown in listing 4.5.

Die approbierte gedruckte Originalversion dieser Diplomarbeit ist an der TU Wien Bibliothek verfügbar
The approved original version of this thesis is available in print at TU Wien Bibliothek.
TU Bibliothek Your knowledge hub WIEN

Table 2.2: Example dataframe. The particle mask distinguishes between "EVs", labelled as 1.0, and "non-EVs", labelled as 2.0.

height	phase	particle_mask
3.360647	17.923920	2.0
3.533748	16.997755	2.0
3.587121	18.133762	2.0
3.425005	17.843719	2.0
	⋮	
11.427134	11.101303	1.0
11.033755	12.330694	1.0

From this training set the LDA could be run, see the code 2.1, and the accuracy of the prediction could be determined using a test set split-off.

Code Listing 2.1: Python code to train the LDA for classifying EV and substrate pixels

```
# convert dataframe to np.array
data = df_hp.values
# last column contains class (y), all other columns are independent variables
X, y = data[:, :-1], data[:, -1]
# ensure X does not contain "object" types
X = X.astype('float32')
X_train, X_test, y_train, y_test = sklearn.model_selection.train_test_split(X
                                        , y, random_state=1)

# instantiate and fit classifier
lda = LinearDiscriminantAnalysis()
lda.fit(X_train, y_train)

# check accuracy
y_hat = lda.predict(X_test)
print("Accuracy score", sklearn.metrics.accuracy_score(y_test, y_hat))
```

Since only two variables (phase and height) are used, it can be shown graphically how the LDA separates the data and distinguishes the between "EV" and "substrate" pixels (see

Die approbierte gedruckte Originalversion dieser Diplomarbeit ist an der TU Wien Bibliothek verfügbar
The approved original version of this thesis is available in print at TU Wien Bibliothek.
TU Bibliothek Your knowledge hub WIEN

fig. 2.19). The combination of phase and height is necessary to obtain a full separation of the vesicles. As already mentioned, vesicles are both higher and softer, which is reflected here.

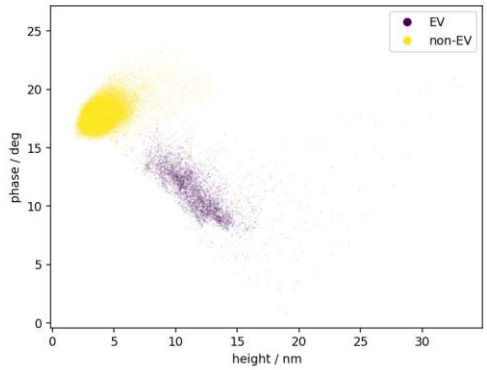

Figure 2.19: Data after the LDA distinguishes between "EV" and "non-EV" by using "phase" and "height" as variables

Furthermore, the hyperplane can be shown graphically, after calculating the prediction for the data (code see 4.7). In figure 2.20, it can be clearly seen that in this case most of the data is well separated, yet with small overlaps.

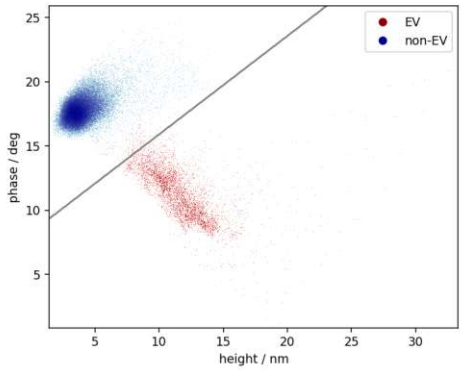

Figure 2.20: Calculated hyperplane of the sample data, small overlaps of 'EV' into 'non-EV' are visible

The LDA classifier can be applied to the image to show areas assigned to EVs and substrate. This LDA-treated data can be used to plot an image, where you should exactly

Die approbierte gedruckte Originalversion dieser Diplomarbeit ist an der TU Wien Bibliothek verfügbar
The approved original version of this thesis is available in print at TU Wien Bibliothek.
TU Bibliothek Your knowledge hub WIEN

see which data point is an EV and which is not. The figure in 2.21 shows this.

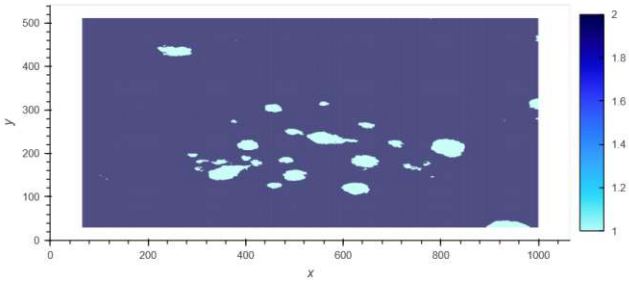

Figure 2.21: Predicted EVs in the data by the LDA classifier

Segmentation - Classifier Prediction Probability The LDA itself has a hard cut-off for class assignment. Each sample is either in class A or B, even if it lies very close to the separating hyperplane. In this dataset, substrate and EV point clouds show some overlap. While just from height and phase data it is therefore not possible to perfectly separate these classes the location of pixels can help to better distinguish, meaning if a pixel is close to hyperplane but spatially close to many other pixels that are determined to be "EV" then it is likely also an "EV" pixel. We can model the probability of class assignment in the LDA by calibrating the classifier: a logistic regression or an sigmoid regressor is fitted to the decision function to predict the class assignment probability. This procedure was performed as outlined in LDA classifier using `sklearn.calibration.CalibratedClassifierCV` [56], see 2.2:

Code Listing 2.2: Python code to run the different LDA aproaches

```
# With no calibration
prob_pos_clf = lda.predict_proba(X_test)[:, 1]

# With isotonic calibration
clf_isotonic = CalibratedClassifierCV(lda, cv=2, method="isotonic")
clf_isotonic.fit(X_train, y_train)
prob_pos_isotonic = clf_isotonic.predict_proba(X_test)[:, 1]
```


Die approbierte gedruckte Originalversion dieser Diplomarbeit ist an der TU Wien Bibliothek verfügbar
The approved original version of this thesis is available in print at TU Wien Bibliothek.
TU Bibliothek Your knowledge hub WIEN

```
# With sigmoid calibration
clf_sigmoid = CalibratedClassifierCV(lda, cv=2, method="sigmoid")
clf_sigmoid.fit(X_train, y_train)
prob_pos_sigmoid = clf_sigmoid.predict_proba(X_test)[:, 1]
```

The best calibration, the line that most closely follows the diagonal labelled "perfectly calibrated", was selected using plots like the one shown in fig. 2.22.

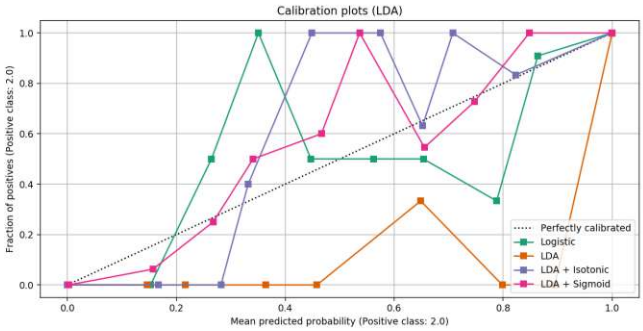

Figure 2.22: Comparison of the different LDA models

Segmentation - Watershed and Vesicle Extraction After choosing the best LDA approach, the segmentation, as described in section 2.4.1, can be performed with the code shown in 2.3. The parameters for the segmentation could be modified via `markers[(vesikel['proba_cl2']>.1)]=background` and `markers[(vesikel['proba_cl1']>.95)]=foreground`.

Code Listing 2.3: Python code to run the segmentation

```
data = df_hp_all_dropna.values
vesikel = xr.Dataset.from_dataframe(df_hp_all_dropna).transpose("y",...)
edges = filters.sobel(vesikel['height'])

#defining the parameters
markers = np.zeros_like(vesikel['height'])
foreground, background = 1, 2
markers[ (vesikel['proba_cl2']>.1)]  = background
```


Die approbierte gedruckte Originalversion dieser Diplomarbeit ist an der TU Wien Bibliothek verfügbar
The approved original version of this thesis is available in print at TU Wien Bibliothek.
TU Bibliothek Your knowledge hub WIEN

```
markers[(vesikel['proba_cl1']>.95) ] = foreground

#performing watershedding and labelling
ws = watershed(edges, markers)
seg1 = label(ws == foreground, )

#declaring the found vesicle into a variable
expanded = expand_labels(seg1, distance=1)
```

In the resulting array `expanded` each pixel either is numbered with an integer or marked "not a number" (NaN). The integer numbers denote membership of a specific EV, meaning that all pixels numbered 10 belong to vesicle 10. `expanded` can also be used to select only pixels that are located on vesicles in the AFM-IR spectral images by only selecting pixels in the spectral image where `expanded` is not `NaN` (see fig. 2.23).

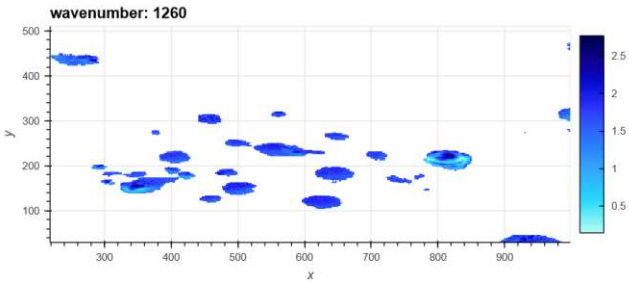

Figure 2.23: Plot of the AFM-IR signal at 1260 cm^{-1} only on pixels that are on an EV, as found by segmentation.

Per-EV Evaluation The segmentation created in the the previous section was used to select all pixels belonging to each EV by using `spectra_per_pixel=stacked_selected.TapIR.reindex_like(expanded_da).where(expanded_da!=0).stack(sample=("x","y")).dropna("sample")`. These can be analyzed using chemometric tools to find common trends, such as PCA (introduced in section 2.4.4).

Die approbierte gedruckte Originalversion dieser Diplomarbeit ist an der TU Wien Bibliothek verfügbar
The approved original version of this thesis is available in print at TU Wien Bibliothek.
TU Bibliothek Your knowledge hub WIEN

Code Listing 2.4: Python code to run the PCA

```
X = spectra_per_pixel.reset_coords(set(spectra_per_pixel.coords) - {"
                                        wavenumber", "sample"}, drop=True)
#declaring principal components
n_components = 5

#performing PCA
pca = wrap(PCA(n_components=n_components), reshapes="wavenumber", sample_dim=
                                        "sample")
pca.fit(X)

#Claculating scores for the PCA
scores = pca.transform(X).rename(wavenumber="PC").assign_coords(PC=np.arange(
                                        n_components))
```

The interpretation of scores and loadings will be explained more detailed in results chapter 3.

Vesicle Sizes The size of vesicles was also automatically determined from AFM-IR images. This allows to study correlations between vesicle size and composition. Size was determined by numerically integrating the height image in all pixels belonging to a vesicle using the following function:

```
from scipy.interpolate import RectBivariateSpline

def integrate(gh, del_x, del_y):
    """
    integrates pixel belonging to a selected area.

    gh: xarray with stacked dimensions x and y
    del_x: pixel pitch along x dimension (in length unit)
    del_y: pixel pitch along y dimension (in length unit)
```


Die approbierte gedruckte Originalversion dieser Diplomarbeit ist an der TU Wien Bibliothek verfügbar
The approved original version of this thesis is available in print at TU Wien Bibliothek.
TU Bibliothek Your knowledge hub WIEN

```
    returns
    -------

    xarray.DataArray (single element) containing the 2D integral
    """
    arr= gh.unstack("stacked_x_y").sortby("x").sortby("y")
    # replace all nans (pixel not in EV, but required to make image
                                            rectangular)
    # with 0
    arr = arr.where(~np.isnan(arr), 0)
    interp = RectBivariateSpline(arr.x.to_numpy()*del_x,
                                 arr.y.to_numpy()*del_y,
                                 arr.to_numpy(),
                                 kx=1, ky=1, )
    return xr.DataArray(interp.integral(arr.x.min()*del_x,
                                        arr.x.max()*del_x,
                                        arr.y.min()*del_y,
                                        arr.y.max()*del_y))
```

The height images is then grouped by EV number (from `expanded`) and `integrate` is applied to each group (see listing 2.5).

Code Listing 2.5: Python code for the size distribution

```
group_height = height.reindex_like(expanded_da).groupby(expanded_da)
vesicle_volume = group_height.map(integrate,
                    args=
                    (1000*height.Xpos.diff("x").median().to_numpy(),
                    1000*np.abs(height.Ypos.diff("y").median().to_numpy()))
                    ).isel(group=slice(1,None))
spectra_volume = xr.Dataset({"spectra":vesicle_groups.mean(dim="sample"), "
                                        volume":vesicle_volume })
```


Die approbierte gedruckte Originalversion dieser Diplomarbeit ist an der TU Wien Bibliothek verfügbar
The approved original version of this thesis is available in print at TU Wien Bibliothek.
TU Bibliothek Your knowledge hub WIEN

Figure 2.24 shows a typical result of the correlation of vesicle size and absorption signal. Further interpretation can be seen in chapter 3.

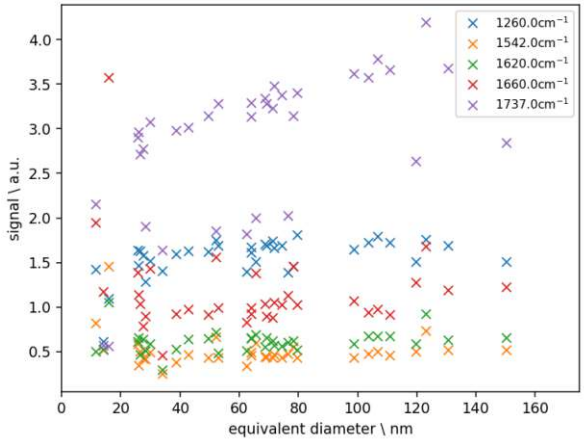

Figure 2.24: Plot of the size comparison

Die approbierte gedruckte Originalversion dieser Diplomarbeit ist an der TU Wien Bibliothek verfügbar
The approved original version of this thesis is available in print at TU Wien Bibliothek.
TU Bibliothek Your knowledge hub WIEN

Die approbierte gedruckte Originalversion dieser Diplomarbeit ist an der TU Wien Bibliothek verfügbar
The approved original version of this thesis is available in print at TU Wien Bibliothek.

CHAPTER 3

Results and Discussion

3.1 Dilution Adjustment

To be able to use the protocol from chapter 2, the correct sample quantity still had to be determined to achieve a high enough number of vesicles per unit area to allow imaging a large number of vesicles within. For this purpose, various dilutions were tested. The next sections show the results of these measurements.

3.1.1 Direct Deposition without Incubation Chamber

In the first measurement, the established protocol has been followed. The sample had been used without further dilution and only 10 µL, without incubation chambers or diffusion time. One particle was found that matched the expected size and shape to be an EV. To verify the particle's chemistry AFM-IR spectra were taken. The first spectrum can be seen in figure 3.1. Additionally, also the location of the tip can be seen. The spectrm compares well to a bulk spectrum of EVs (taken from [15]), with few differences that will be discussed below.

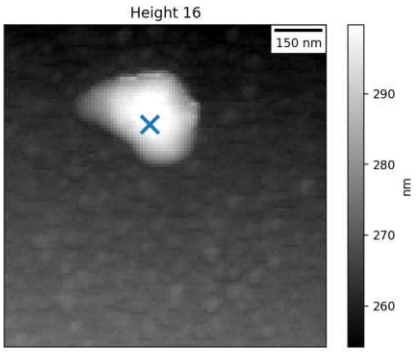

(a) Location of the tip

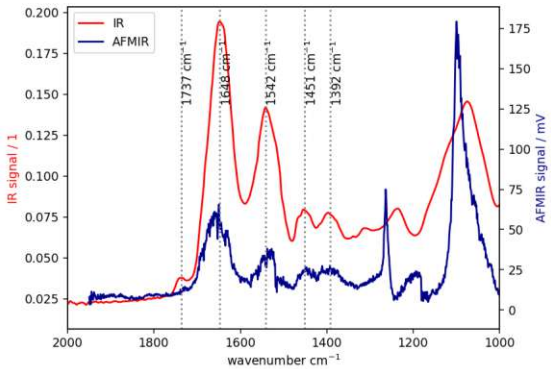

(b) Obtained Spectrum at that location

Figure 3.1: (a) Location where the tip was (b) AFM-IR and IR spectra comparison

In these spectra the amide I at 1648 cm^{-1}[57, 15] and amide II at 1542 cm^{-1}[57, 15] can be seen. These bands belong to protein structures and since EVs can contain proteins in their membrane as cargo, it is very likely to see these bands in the spectrum. The CH_2 bending of lipidic acyl chains at 1451 cm^{-1}can also be associated with proteins [15]. At 1392 cm^{-1}a COO^- symmetric stretch can be seen, which is assigned to fatty acids and aminoacids [57]. The saturated C=O stretch at 1737 cm^{-1}[57, 15], which is very small but visible, is associated with the lipid bi-layer of the EVs. As the cell wall is made out of these, it is very likely linked to it.

The bands at which the spectrum differs from the bulk spectrum can be attributed to

Die approbierte gedruckte Originalversion dieser Diplomarbeit ist an der TU Wien Bibliothek verfügbar
The approved original version of this thesis is available in print at TU Wien Bibliothek.
TU Bibliothek Your knowledge hub WIEN

the substrate and the cantilever. There is a wide band at around 1000 $cm^{-1}$to 1150 cm^{-1}. This is the silicon substrate [58]. Also at around 1260 cm^{-1}there is a significant peak. This peak can be associated with the used cantilever [58, 59]. To confirm that only the found vesicle produced the shown spectrum, another spectrum was taken next to the vesicle, on the substrate. This is shown in figure 3.2.

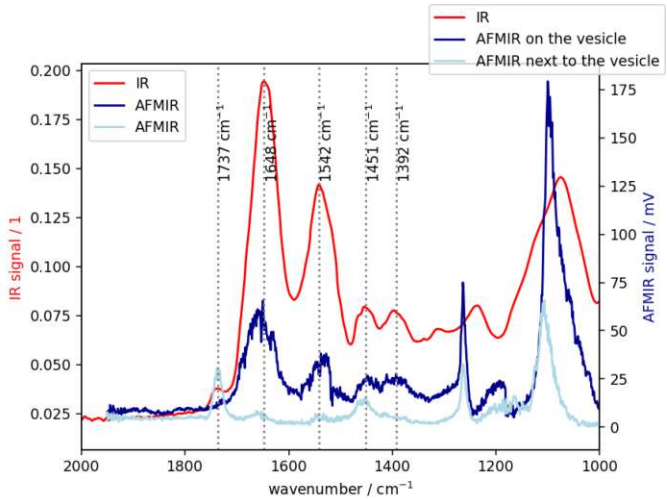

Figure 3.2: Comparison of the IR measurement (red) with AFM-IR spectrum on the vesicle (dark blue) and next to the vesicle (light blue). The found vesicle (dark blue) has the same bands as the IR measurement (red), in contrast to the measurement next to the vesicle (blue).

It can be seen that none of the expected bands are in the measurement next to the vesicle, but the bands at 1000 cm^{-1} to 1150 cm^{-1} and 1260 $cm^{-1}$are still visible.

In this first iteration, it was shown that it is possible to capture the EVs via the protocol described in chapter 2. It was also shown, that without incubation chambers and sufficient diffusion time the surface concentration is low.

3.1.2 Addition of Incubation Chamber

In the second measurement, an incubation chamber was added and the sample was incubated for 52 h to allow for diffusion to the surface. Two difference dilutions of the sample with PBS were tested: 1:2 and 1:50 to investigate the required sample concentration to

Die approbierte gedruckte Originalversion dieser Diplomarbeit ist an der TU Wien Bibliothek verfügbar
The approved original version of this thesis is available in print at TU Wien Bibliothek.

collect a large number of EVs per unit substrate area without overcrowding or stacking of EVs.

3.1.3 1:2 dilution

For the 1:2 diluted sample, a total of 14 spectra were taken. All the spectra can be seen in figure 3.3. It must also be mentioned that the laser power was set very high for this measurement, up to 100 %.

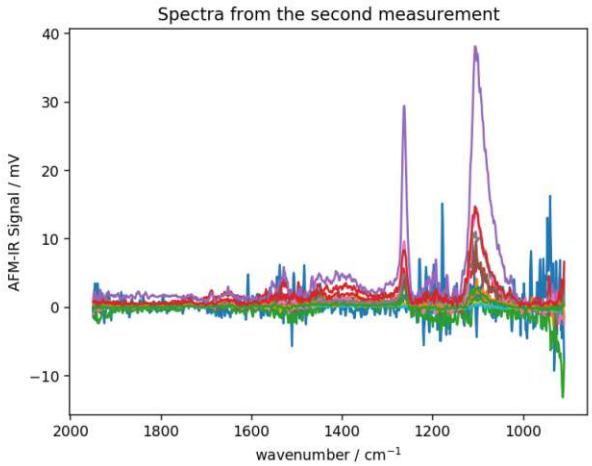

Figure 3.3: All spectra taken from the second measurement

The bands from the substrate and cantilever can be seen in all of the spectra. Besides that, the noise is also recognisable in some of the spectra taken. The same bands, as in figure 3.1, are still visible in some of the spectra. To have a deeper insight, individual spectra are depicted with the location where they were taken from. Figure 3.4 shows a typical spectrum. The bulk EV spectrum is included every time for comparison.

In the spectrum in fig. **??** all the bands, which were already identified in section 3.1.1, can be seen and the found vesicle is clearly visible in the AFM image. Furthermore, the circle, which was printed onto the substrate, can also be seen. Additionally, it is also

Die approbierte gedruckte Originalversion dieser Diplomarbeit ist an der TU Wien Bibliothek verfügbar
The approved original version of this thesis is available in print at TU Wien Bibliothek.
TU Bibliothek Your knowledge hub WIEN

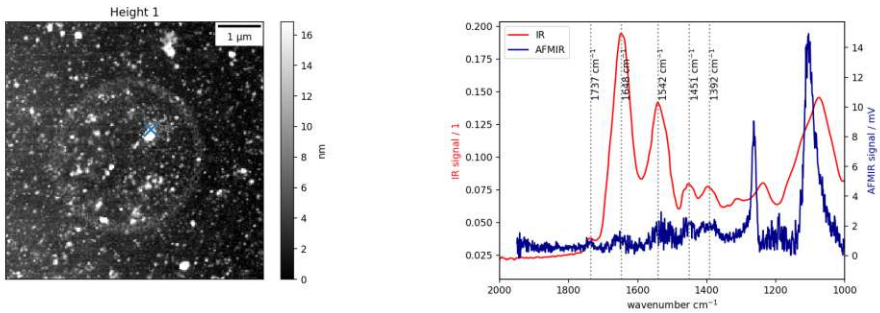

(a) Location of the tip (b) Obtained Spectrum at that location

Figure 3.4: AFM-IR spectrum taken on a vesicle showing weak bands corresponding to the vesicle. (a) Location where the tip was (b) AFM-IR and IR spectra comparison

apparent that the vesicle sticks onto substrate inside the antibody functionalized circular area. The signal from the AFM-IR is not as high as in 3.1, although the laser power has been very high. Nevertheless, the same can be said for this vesicle as about the vesicle in section 3.1.1. In order to verify, that this found signal can only be seen on the vesicle and not anywhere on the circle, the figure 3.5 shows a measurement nearby the vesicle. None of the expected bands can be seen. In fact only the substrate and the signal from the cantilever are visible.

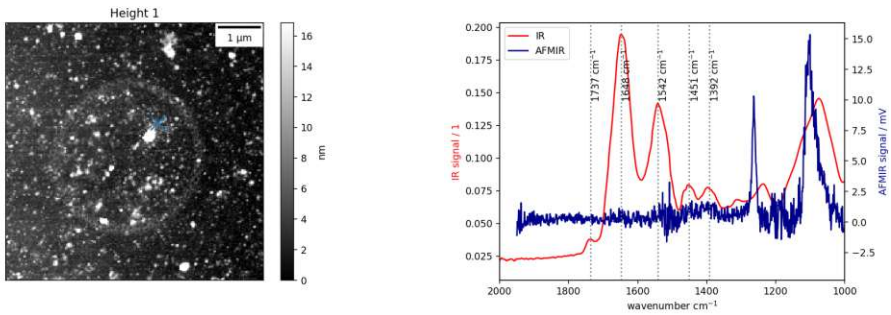

(a) Location of the tip (b) Obtained Spectrum at that location

Figure 3.5: AFM-IR spectrum taken to the side of a vesicle showing only bands assigned to the substrate and the AFM tip. (a) Location where the tip was (b) AFM-IR and IR spectra comparison

An example of a spectrum that shows vesicle bands but with a high noise level can be seen

Die approbierte gedruckte Originalversion dieser Diplomarbeit ist an der TU Wien Bibliothek verfügbar
The approved original version of this thesis is available in print at TU Wien Bibliothek.
TU Bibliothek Your knowledge hub WIEN

in figure 3.6. All the bands, amide I, amide II, COO^- symmetric stretch, CH_2 bending of lipidic acyl chains and C=O stretch, can be seen. The noise level in these spectrum is high in comparison to the band height, for example, the bands at 1542 $cm^{-1}$and 1451 $cm^{-1}$are strongly overlapped.

Another problem that could be discovered at a circle was that the phase image seemed densely packed with vesicles. This can be seen in figure 3.7.

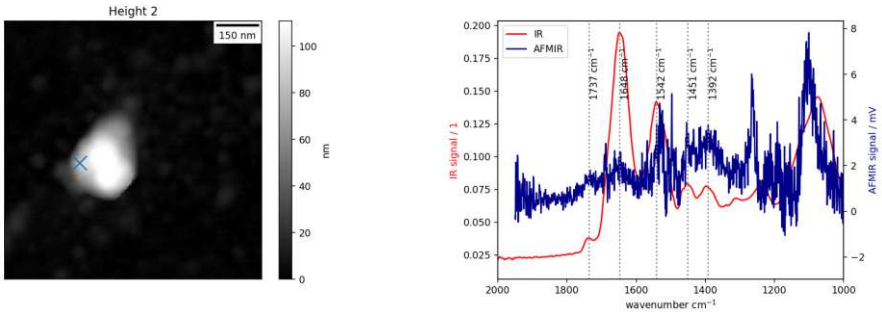

(a) Location of the tip (b) Obtained Spectrum at that location

Figure 3.6: A spectrum taken on a vesicle. The spectrum has a high noise level but nevertheless bands assigned to the vesicle can be made out. (a) Location where the tip was (b) AFM-IR and IR spectra comparison

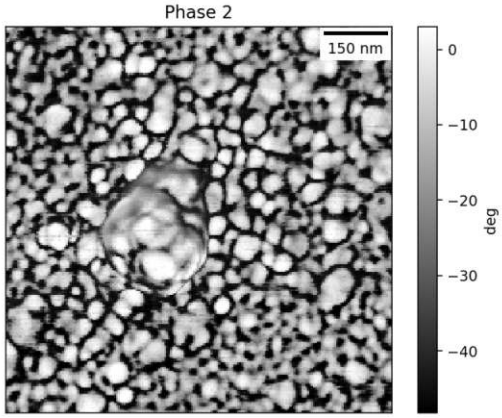

Figure 3.7: Phase image with a overload of vesicles

The topography images of this sample (see figs.3.6 to 3.4) show few, well spaced vesicles.

Die approbierte gedruckte Originalversion dieser Diplomarbeit ist an der TU Wien Bibliothek verfügbar
The approved original version of this thesis is available in print at TU Wien Bibliothek.
TU Bibliothek Your knowledge hub WIEN

However, looking at the phase image (see fig. 3.7) many contiguous soft areas can be made out, suggesting that the substrate was overloaded. They appear to stick together and overcrowd the printed circle.

3.1.4 50:1 dilution

Unfortunately, something went wrong during the execution of the protocol with the 50:1 dilution and no printed circles could be found on the substrate. Multiply large topography and phase images (20 µm×20 µm) were collected. They are depicted in figure 3.8. The imaged areas are large enough that at least one antibody stamped circle should be visible, if they were present.

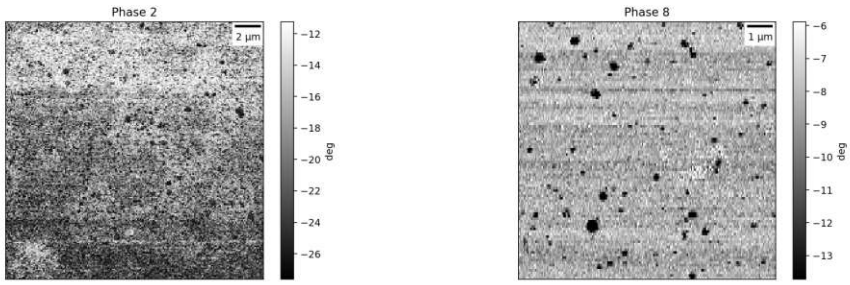

(a) Phase image of the sample (b) Phase image of the sample

Figure 3.8: Phase images from the 50:1 diluted sample showing no printed circles

As a result, no spectra and no AFM-IR imaging has been made.

3.1.5 Adjusted Sample Dilution (1:10)

The third measurement was performed with a 1:10 dilution as the 1:2 seemed a bit overloaded in some spots (see figure 3.7). As usual, the experimental protocol was followed and the substrate searched for a circle, where the spectra could been taken. The sample was found to show a large number of vesicles which in most cases were clearly spaced apart (see fig. 3.10). On this sample, in total, 34 spectra were taken, which are

Die approbierte gedruckte Originalversion dieser Diplomarbeit ist an der TU Wien Bibliothek verfügbar
The approved original version of this thesis is available in print at TU Wien Bibliothek.
TU Bibliothek Your knowledge hub WIEN

shown in figure 3.9. The laser power ranged from 8.81 % up to 80.4 %.

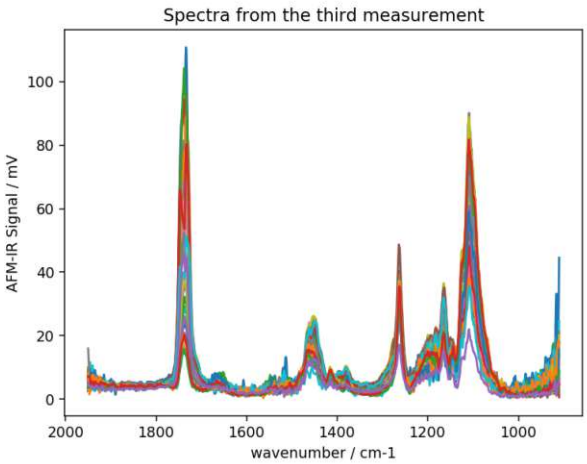

Figure 3.9: Overview of all AFM-IR spectra taken on the sample incubated with a 1:10 diluted vesicle suspension.

In most spectra the band at 1737 cm^{-1} appears to be very strong and there are also large band intensities at 1392 cm^{-1} and 1451 cm^{-1}. This suggests, that mostly the lipid bi-layer of the cell wall has been found. However, there are also some spectra that have the bands at 1542 cm^{-1} and 1648 cm^{-1}, which can be assigned to proteins . To have a better insight, the spectra are again compared to the location where they have been taken.

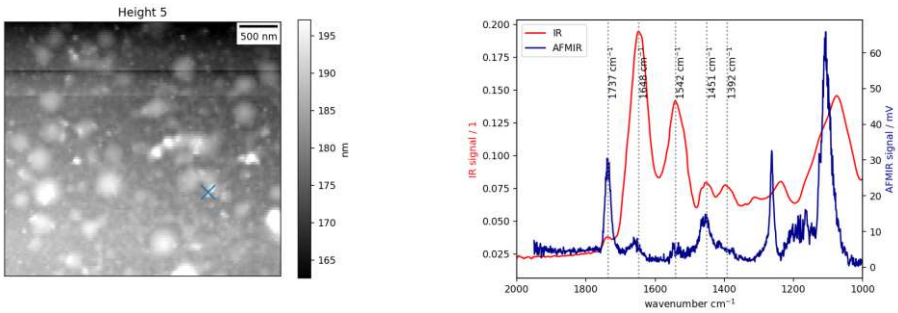

(a) Location of the tip (b) Obtained Spectrum at that location

Figure 3.10: (a) Location where the tip was (b) AFM-IR and IR spectra comparison

In figure 3.10, a spectrum is shown that exhibits contributions from bands that can be

Die approbierte gedruckte Originalversion dieser Diplomarbeit ist an der TU Wien Bibliothek verfügbar
The approved original version of this thesis is available in print at TU Wien Bibliothek.
TU Bibliothek Your knowledge hub WIEN

assigned to proteins. In this spectrum, the strong C=O stretch at 1737 cm^{-1} and also the amide I band at around 1648 cm^{-1} can be seen. The amide II band is also visible at around 1542 cm^{-1}, and the band at 1451 cm^{-1} suggests that this is in fact an EV. There is also a small band at 1414 cm^{-1}, which could be associated with a stretching of C−N [57], that can also be assigned to a protein.

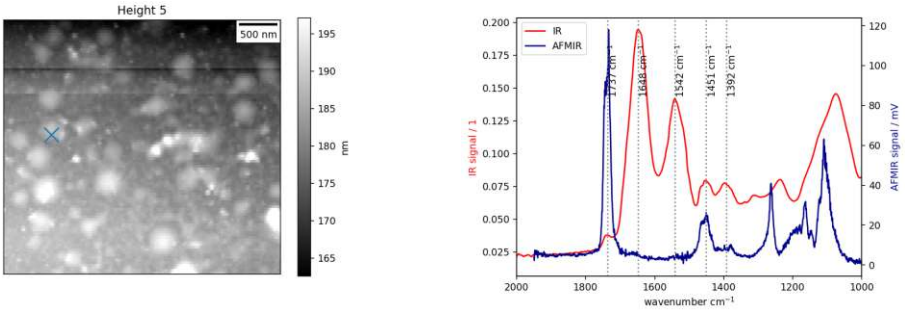

(a) Location of the tip (b) Obtained Spectrum at that location

Figure 3.11: AFM-IR spectrum showing high bands assigned to lipids and low (or no) contributions from proteins. (a) Location where the tip was (b) AFM-IR and IR spectra comparison

Another potential vesicle near the first one in figure 3.10 is shown in figure 3.11. In contrast to the previous spectrum, only the bands at 1737 cm^{-1}, 1451 cm^{-1} and around 1392 cm^{-1} are visible. The amide I and II bands are hardly visible (or not present) and are much weaker than the carbonyl stretch band. This could mean that this specific vesicle does not have any (or very low) protein content. It could mean that when the vesicle dried out its protein cargo precipitated and are where concentrated in a small part of the vesicle. Due to the high spatial resolution of AFM-IR, if the tip was placed outside this small part while the spectrum was taken, they would thus not be detected.

The effect of this high spatial resolution is also seen in the next example (see figure 3.12) . Here a small change in sample position leads to a large change in the spectrum. In the first spectrum spectrum (see fig. 3.12b), only the carbonyl band at 1737 cm^{-1} and the CH_2 bending of lipidic acyl chains at 1451 cm^{-1} can be seen. However, when the tip is

Die approbierte gedruckte Originalversion dieser Diplomarbeit ist an der TU Wien Bibliothek verfügbar
The approved original version of this thesis is available in print at TU Wien Bibliothek.
TU Bibliothek Your knowledge hub WIEN

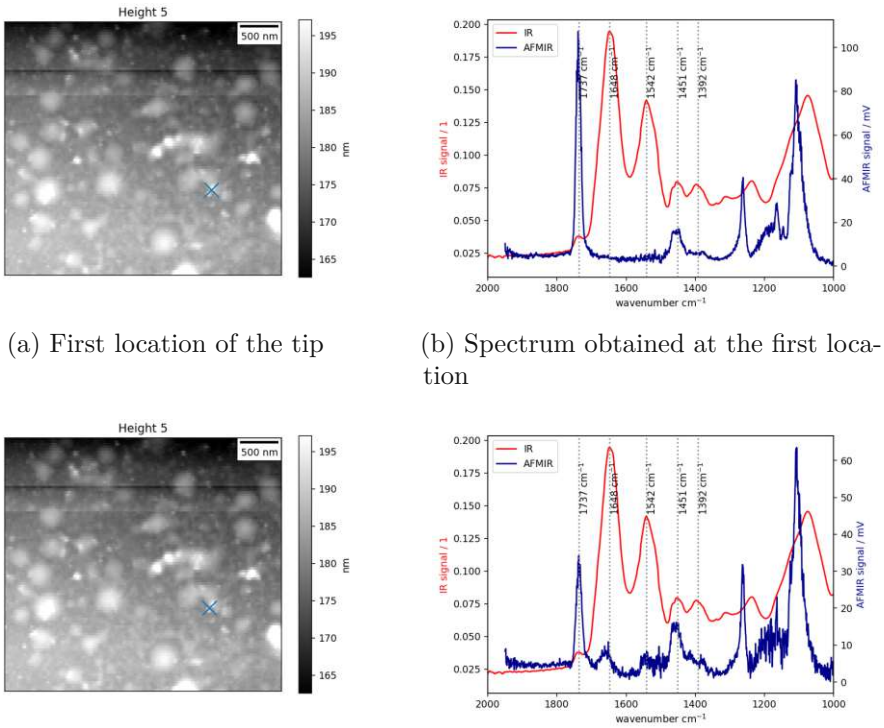

(a) First location of the tip

(b) Spectrum obtained at the first location

(c) Second locations of the tip

(d) Spectrum obtained at the second location

Figure 3.12: AFM-IR spectra taken on the same vesicle with slightly different positions. The first spectrum (b) is dominated by lipid bands, while in the second spectrum (d) amide bands are clearly visible. Location of the tip (a), (c) and their respective spectra (b), (d)

slightly moved but still placed within the same vesicle amide bands are also observed (see fig. 3.12d). This shows, that the composition seen in AFM-IR spectra can change within a single vesicle.

This third measurement has also shown that a dilution of 1:10 is most appropriate for conducting future experiments with this sample concentration of 10^8 particles/mL.

Die approbierte gedruckte Originalversion dieser Diplomarbeit ist an der TU Wien Bibliothek verfügbar
The approved original version of this thesis is available in print at TU Wien Bibliothek.
TU Bibliothek Your knowledge hub WIEN

3.2 Structure and Chemical Composition of Individual EVs

As was demonstrated in the previous section, the spatial resolution of AFM-IR (≈20 nm) means that single point spectra taken of vesicles are not representative of a whole vesicle. Additional information about the chemical composition of the vesicle can be acquired using AFM-IR imaging. However, as AFM-IR imaging only record the AFM-IR signal at one specific wavenumber per image, in order to characterize vesicles efficiently, the wavenumbers described in section 3.1 and wavenumbers from Ramos-Garcia et al. [15] were used. Marker bands for lipids and proteins were selected. Furthermore the 1260 cm^{-1} band assigned to the silicon oil on the cantilever was imaged as "internal intensity standard". All imaged bands can be seen in table 3.1.

Table 3.1: Wavenumbers used for AFM-IR imaging

wavenumber in cm^{-1}	spectral assignment
1260	CH_3 deformation vibration of $Si-CH_3$, cantilever
1392	COO^- symmetric stretch
1451	CH_2 bending of lipidic acyl chains
1542	Amide II
1646	Amide I
1737	saturated C=O stretch

To get a deeper insight into the AFM-IR data, various processing steps were carried out. The concept of these steps are explained in 2.4 and an example data evaluation has also been performed.

3.2.1 AFM-IR Imaging

AFM-IR images taken from the first measurement can be seen in figure 2.13. Here, the PCC, described in section 2.4.2, was used to align the different AFM-IR images and to be able to see the difference in the wavenumbers used. The main problem in this iteration was that the image size used was too small (1x1 µm image). Thus the vesicle does not

Die approbierte gedruckte Originalversion dieser Diplomarbeit ist an der TU Wien Bibliothek verfügbar
The approved original version of this thesis is available in print at TU Wien Bibliothek.
TU Bibliothek Your knowledge hub WIEN

stay within the image section for all images due to piezo creep and change of the ambient temperature.

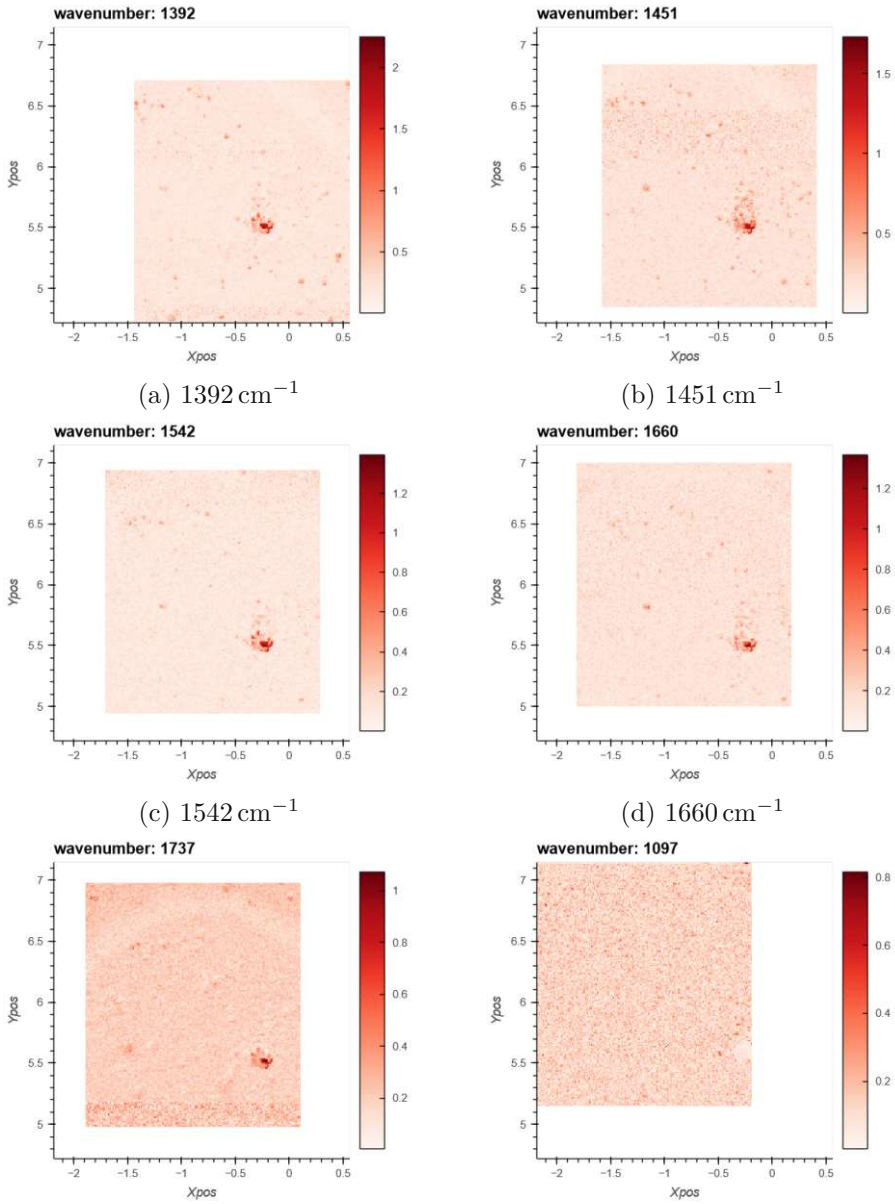

(a) 1392 cm^{-1} (b) 1451 cm^{-1}

(c) 1542 cm^{-1} (d) 1660 cm^{-1}

(e) 1737 cm^{-1} (f) 1097 cm^{-1}

Figure 3.13: AFM-IR images of the second vesicle sample (1:2 dilution, see also section 3.1.3 for spectra and topography images) with the respective wavenumbers (a) 1392 cm^{-1} (b) 1451 cm^{-1} (c) 1535 cm^{-1} (d) 1660 cm^{-1} (e) 1737 cm^{-1} (f) 1097 cm^{-1}

Die approbierte gedruckte Originalversion dieser Diplomarbeit ist an der TU Wien Bibliothek verfügbar
The approved original version of this thesis is available in print at TU Wien Bibliothek.
TU Bibliothek Your knowledge hub WIEN

The AFM-IR images from the second measurements can be seen in figure 3.13. The large vesicle does have signals at the identified wavenumbers, but some small particles also show some signal. With the help of these AFM-IR images, the smaller vesicle-like particles can also be characterized via LDA and PCA. This will be done in section 3.2.2.

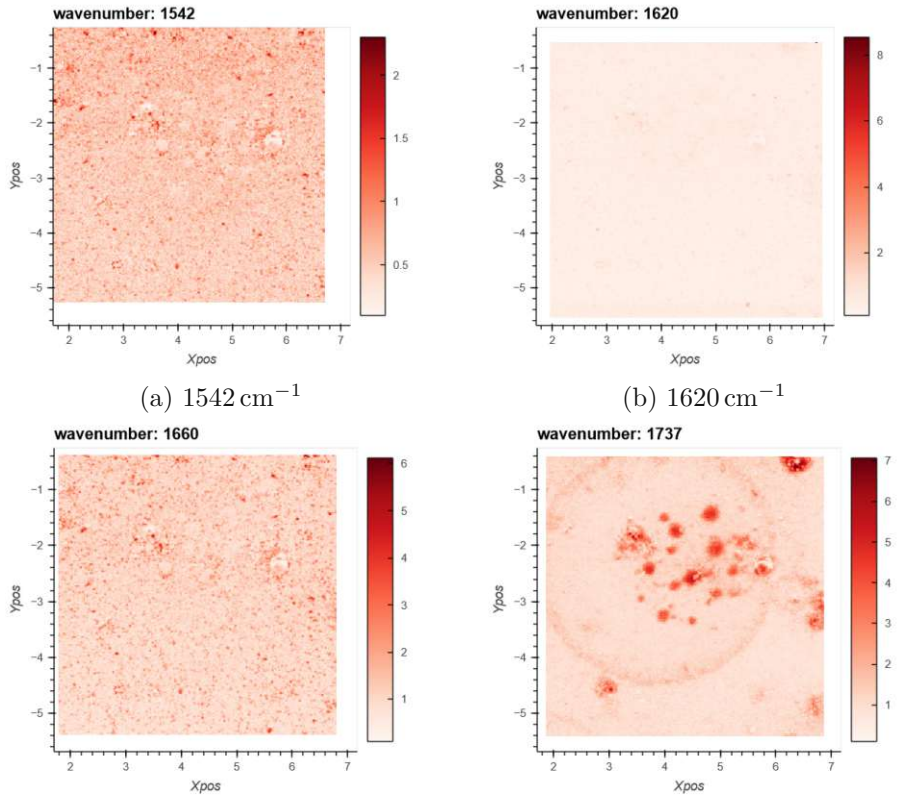

(a) 1542 cm^{-1} (b) 1620 cm^{-1}

(c) 1660 cm^{-1} (d) 1737 cm^{-1}

Figure 3.14: AFM-IR images of the sample incubated with 1:10 diluted vesicle suspension. Imaging was carried out the following (a) 1542 cm^{-1} (b) 1620 cm^{-1} (c) 1660 cm^{-1} and (d) 1737 cm^{-1}

In figure 3.14 the AFM-IR images from the third measurement (1:10 diluted sample; incubated with incubation chamber) can be seen. As expected, the wavenumber 1737 cm^{-1} (see 3.1.5) shows the image with the highest signal. Nevertheless, it can also be seen that at 1660 cm^{-1} some signal can be found, which would match with the assumptions that EVs have different compositions. The same applies to wavenumber 1542 cm^{-1}, that signal

Die approbierte gedruckte Originalversion dieser Diplomarbeit ist an der TU Wien Bibliothek verfügbar
The approved original version of this thesis is available in print at TU Wien Bibliothek.
TU Bibliothek Your knowledge hub WIEN

can be found in different locations, and thus implying different chemical composition. At 1620 cm^{-1}, no signal can be seen, which matches all spectra seen in 3.9. Again, it is possible to look deeper into this measurement, which will be done in section 3.2.2.

3.2.2 Data Analysis

Data Analysis of the Second Measurement

The data analysis was carried out as in the example data evaluation, see section 2.4.5. Below only the sample specific inputs for analysis are shown. Details and general explanation can be found in chapter 2.4.5. It must also be mentioned that the data from the second measurement, the 1:2 dilution, was used here, which was not optimized.

After loading the measurement file and selecting the correct images, a mask for training the LDA for segmentation was created. In figure 3.15 the mask can be seen. In the mask only vesicles that appear in the topography and the phase images were marked as "vesicle", many different areas were selected as "substrate" to create a representative sample.

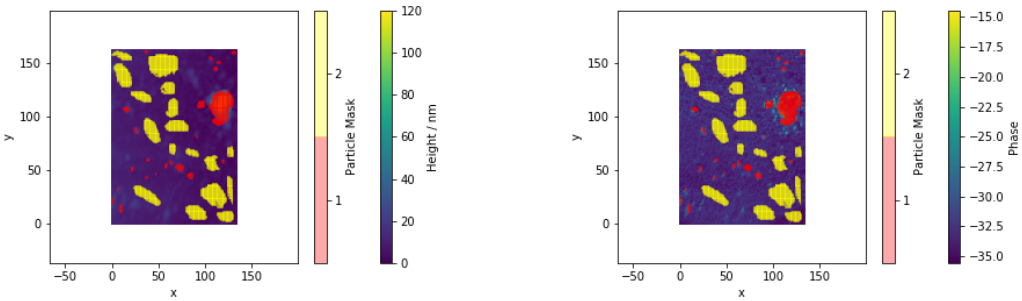

(a) Height image with mask (b) Phase image with mask

Figure 3.15: Mask used for training the LDA. (a) Mask plotted on top the height image and on top of the (b) phase image with marked "EVs" (red) and "non-EVs" (yellow)

With this data, the LDA was performed and the accuracy score was calculated at 0.9377. This means that the data can be distinguished very well. To represent the probability

Die approbierte gedruckte Originalversion dieser Diplomarbeit ist an der TU Wien Bibliothek verfügbar
The approved original version of this thesis is available in print at TU Wien Bibliothek.
TU Bibliothek Your knowledge hub WIEN

of missclassification of point close to the decision hyperplane the LDA was calibrated using a sigmoid approach, since this calibration was closer to the "perfectly calibrated" diagonal than the other approaches (see fig. 3.16).

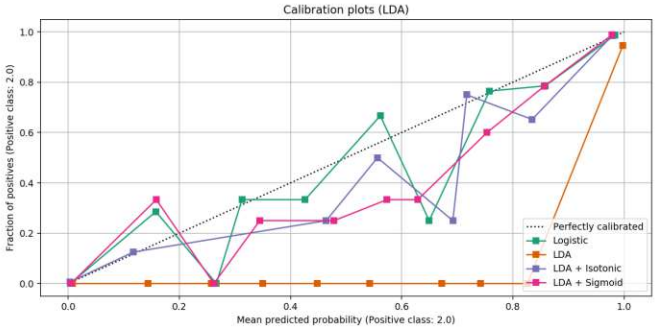

Figure 3.16: Comparison of the different LDA approaches

Now, the segmentation of the data could be performed (see section 2.3) and all the data points associated with EVs could be found. In total, 55 vesicles were found by the algorithm. In figure 3.17 the AFM-IR signal measured at different wavenumbers on the vesicles is displayed.

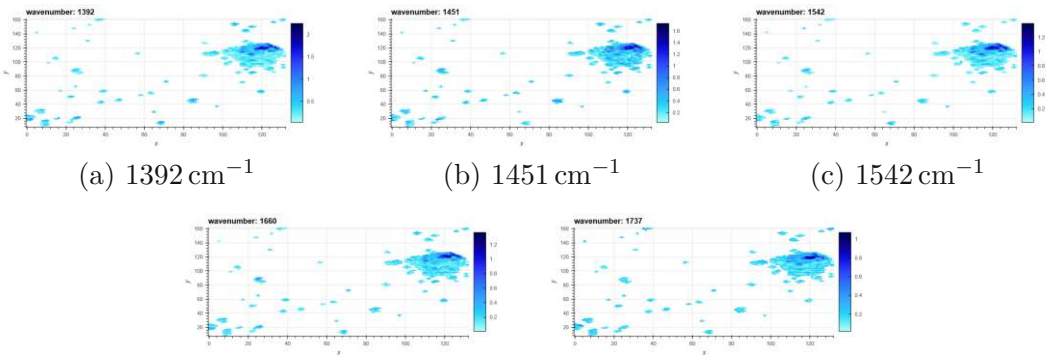

(a) 1392 cm^{-1} (b) 1451 cm^{-1} (c) 1542 cm^{-1}

(d) 1660 cm^{-1} (e) 1737 cm^{-1}

Figure 3.17: Plots of the found EVs at the respective wavenumber **(a)** 1392 cm^{-1} **(b)** 1451 cm^{-1} **(c)** 1542 cm^{-1} **(d)** 1660 cm^{-1} **(e)** 1737 cm^{-1}

These images already show some slight differences in the different wavenumbers. However, it can also be seen that the signals are highly correlated. This is not suprising as thicker parts of a vesicle likely contain a higher amount of all components. In order to

Die approbierte gedruckte Originalversion dieser Diplomarbeit ist an der TU Wien Bibliothek verfügbar
The approved original version of this thesis is available in print at TU Wien Bibliothek.
TU Bibliothek Your knowledge hub WIEN

better visualize changes in composition a PCA (see section 2.4) were performed. The explained variance, which describes how much of the variance is explained by one principal component, can be seen in table 3.2. A high explaine variance typically means that a principal component is "important" whereas very low explained variance means that a principal component is dominated by noise.

Table 3.2: Explained variance for the individual principle components in the second measurement.

Principal Component	Explained Variance
0	0.76206121
1	0.07911964
2	0.04656279
3	0.03643103
4	0.03058734
5	0.02323379
6	0.02200421

It is clear to see that the zeroth principal component has the highest explanatory power out of all principal components in the dataset. To interpret the principal components we look at their loadings plot (see fig. 3.18) which shows how the components correlate with the different wavenumbers of the AFM-IR imaging.

The zeroth principal component correlates positively with all imaged wavenumbers ($1260\,\mathrm{cm}^{-1}$, $1392\,\mathrm{cm}^{-1}$, $1451\,\mathrm{cm}^{-1}$, $1542\,\mathrm{cm}^{-1}$, $1620\,\mathrm{cm}^{-1}$, $1660\,\mathrm{cm}^{-1}$, $1737\,\mathrm{cm}^{-1}$), but it has the weakest loading for 1260 (substrate/cantilever). This can interpreted as the more PC0 there is, the thicker the vesicle is at that pixel. PC1 shows high negative loading for $1392\,\mathrm{cm}^{-1}$ and high positive loading for $1451\,\mathrm{cm}^{-1}$. As $1451\,\mathrm{cm}^{-1}$ can imply asymmetric CH_3 bending modes of the methyl groups of proteins [57] and $1392\,\mathrm{cm}^{-1}$ can be interpreted as a COO^- symmetric stretch. This can mean that this pixel has a weaker contribution from the bands associated with the lipids bi-layer. PC2 correlates negatively at $1392\,\mathrm{cm}^{-1}$, $1542\,\mathrm{cm}^{-1}$ and $1737\,\mathrm{cm}^{-1}$, but positively at $1451\,\mathrm{cm}^{-1}$ and $1660\,\mathrm{cm}^{-1}$. That means PC2 describes the relative abundance of lipids and proteins. A positive score

Die approbierte gedruckte Originalversion dieser Diplomarbeit ist an der TU Wien Bibliothek verfügbar
The approved original version of this thesis is available in print at TU Wien Bibliothek.
TU Bibliothek Your knowledge hub WIEN

Figure 3.18: Loadings plot relating principal components to wavenumbers.

for PC2 means that there is a higher amount of protein at a pixel and a negative score points towards a higher amount of lipid. When loadings for the two wavelengths lying within the amid I bands (1620 cm^{-1} and 1660 cm^{-1}) have opposing signs (such as in PC3) this could indicate as the principal component indicating a difference in secondary structure.

A scores plot plots PCs against each other to find trends or visualize clusters in the data set. Because of the large number of points in this set drawing individual data points would lead to overprinting in denser areas. Therefore, instead a technique called Abstract Rendering or datashading [60] was used. In this approach whenever too many points cluster together their color is adjusted to signify their density. The score plot is depicted

Die approbierte gedruckte Originalversion dieser Diplomarbeit ist an der TU Wien Bibliothek verfügbar
The approved original version of this thesis is available in print at TU Wien Bibliothek.
TU Bibliothek Your knowledge hub WIEN

in figure 3.19.

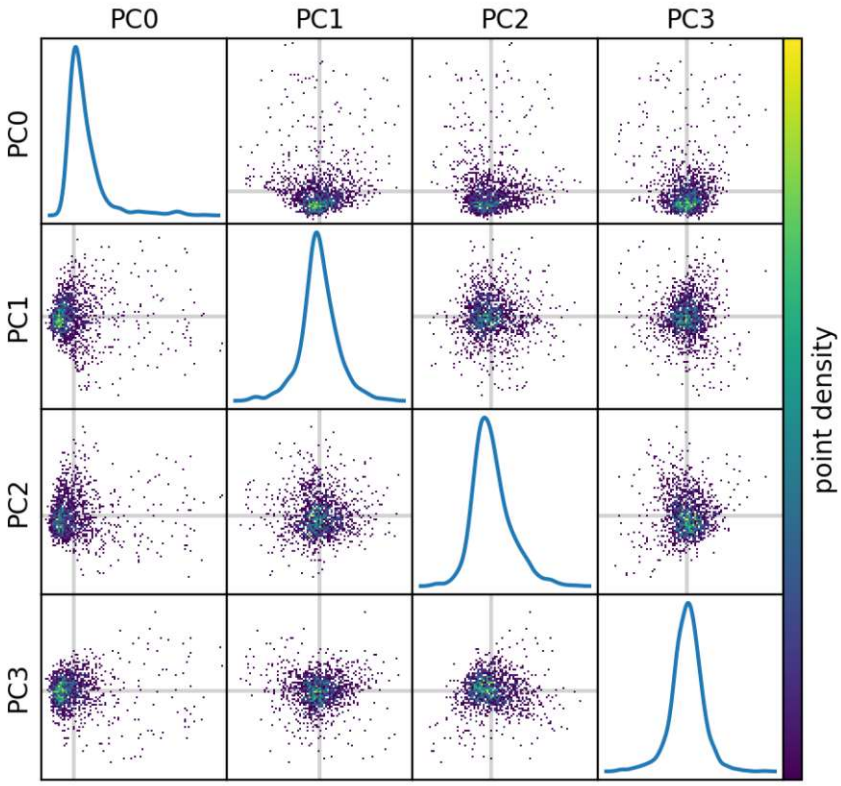

Figure 3.19: Scores plot of PC0 to PC3. Labels on the sides of the plot indicate the plotted scores. Along the diagonal the distribution of each score is depicted as density function. Grey lines indicate scores of 0.

All PCs have a signal maximum of their distribution, with points spreading out from there. The most asymmetric distribution is found in PC0 and PC1. Overall, no clearly distinct pixels or vesicles can be made out.

Die approbierte gedruckte Originalversion dieser Diplomarbeit ist an der TU Wien Bibliothek verfügbar
The approved original version of this thesis is available in print at TU Wien Bibliothek.
TU Bibliothek Your knowledge hub WIEN

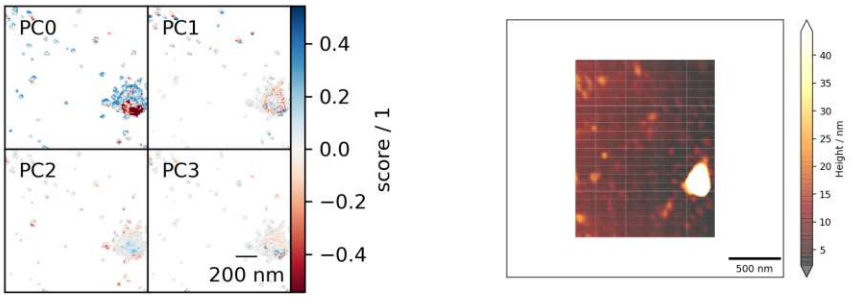

(a) Score Plot (b) Topography Image

Figure 3.20: (a) Score plots applied onto the pixels. Every PC shows up at different pixels, thus underlining the difference in the vesicles. Positive (blue) and negative (red) scores can be seen. (b) topography image of the same area.

In figure 3.20, the scores are plotted onto their corresponding pixels. It is possible to see that in each vesicle, a different PC has a high value, thus implying a different chemical composition. The large vesicle on the lower right side of the image has both very high and very low values for PC0. This likely means that there is an area of relative high lipid content (blue, positive PC0), and an area where higher protein content (red, negative PC0) but compensated by PC1, PC2 and PC3. Most small vesicles mainly show positive scores of PC0. However, interpretation of these images is not straight forward and potentially other chemometric methods could be advantageous.

Image segmentation allows to get per vesicle average "spectra" (averages of the AFM-IR signal across an EV). This allows to see if the EV size has an impact on its the composition. In figure 3.21 AFM-IR signals are plotted against vesicle sizes.

In figure 3.21, an upward trend is seen for all wavenumbers except for $1737\,\mathrm{cm}^{-1}$.

Die approbierte gedruckte Originalversion dieser Diplomarbeit ist an der TU Wien Bibliothek verfügbar
The approved original version of this thesis is available in print at TU Wien Bibliothek.
TU Bibliothek Your knowledge hub WIEN

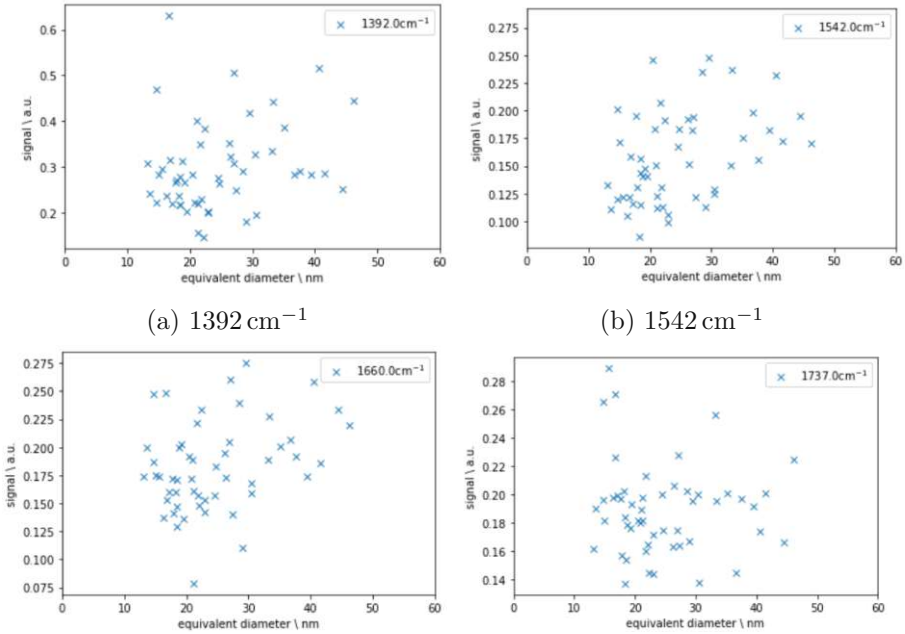

(a) 1392 cm^{-1} (b) 1542 cm^{-1}

(c) 1660 cm^{-1} (d) 1737 cm^{-1}

Figure 3.21: Equivalent diameter plotted against the signal at the respective wavenumbers (a) 1392 cm^{-1} (b) 1542 cm^{-1} (c) 1660 cm^{-1} (d) 1737 cm^{-1}. In all of the plots a positive trend is visible. Note that the very large vesicle was excluded in this diagram.

Data Analysis of the Third Measurement

The data in the third measurement was preprocessed and corrected in the same way as the second measurement (see 2.4.5). A new mask was created for LDA (see fig. 3.22).

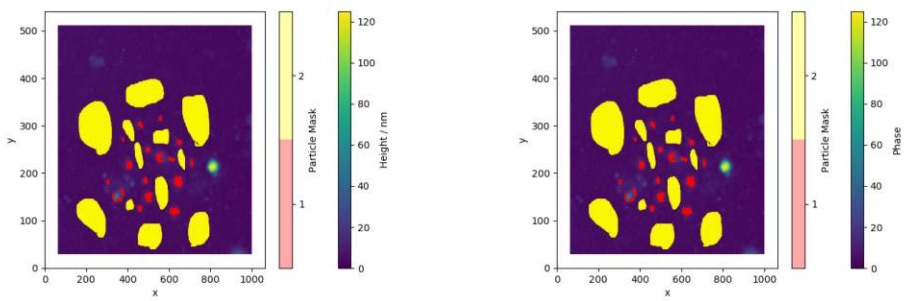

(a) Height image with mask (b) Phase image with mask

Figure 3.22: (a) Mask on the height image and on the (b) phase image with marked "EVs" (red) and "non-EVs" (yellow)

Die approbierte gedruckte Originalversion dieser Diplomarbeit ist an der TU Wien Bibliothek verfügbar
The approved original version of this thesis is available in print at TU Wien Bibliothek.
TU Bibliothek Your knowledge hub WIEN

The performed LDA had an calculated accuracy score of 0.9982 and can thereby distinguish very well between the two selected groups. Different approaches of calibrating the LDA uncertainty have been compared again (see figure 3.23 and the sigmoid approach has been chosen for calibration.

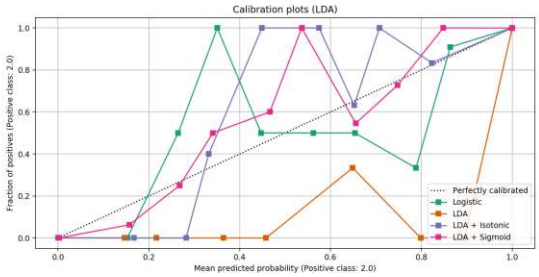

Figure 3.23: Comparison of the different LDA approaches

With the now prepared data, the segmentation could be performed (see listing 2.3). Additionally, the data point, which is associated with EVs, could be found. In total, 35 vesicles were found and these can be seen at different wavenumbers in figure 3.24.

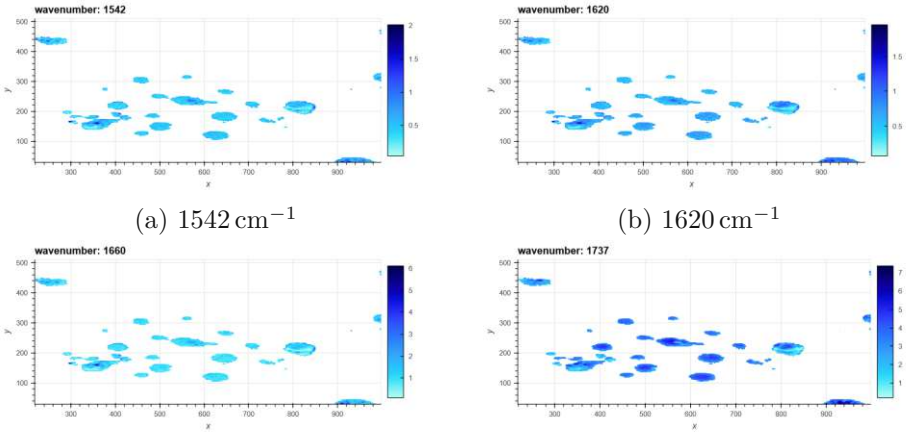

(a) 1542 cm^{-1} (b) 1620 cm^{-1}

(c) 1660 cm^{-1} (d) 1737 cm^{-1}

Figure 3.24: Plots of the found EVs at the respective wavenumbers (a) 1542 cm^{-1} (b) 1620 cm^{-1} (c) 1660 cm^{-1} and (d) 1737 cm^{-1}

It is clear to see that there a differences in different wavenumbers, especially at 1737 cm^{-1}. This also matches with the spectra from section 3.1.5, where a lot of carbonyl signals can be seen. To again have a deeper insight, PCA (see listing 2.4) was performed. The

Die approbierte gedruckte Originalversion dieser Diplomarbeit ist an der TU Wien Bibliothek verfügbar
The approved original version of this thesis is available in print at TU Wien Bibliothek.
TU Bibliothek Your knowledge hub WIEN

explained variance can be seen in table 3.3.

Table 3.3: Explained variance for the individual principle components in the second measurement

Principal Component	Explained Variance
0	0.72966657
1	0.19676131
2	0.04446433
3	0.01979485
4	0.00931293

In table **??** PC0 and PC1 have the highest explanatory power. The loadings plot, which shows how the components correlate with different wavenumbers of the AFM-IR imaging, to interpret the principal components can be seen in 3.25.

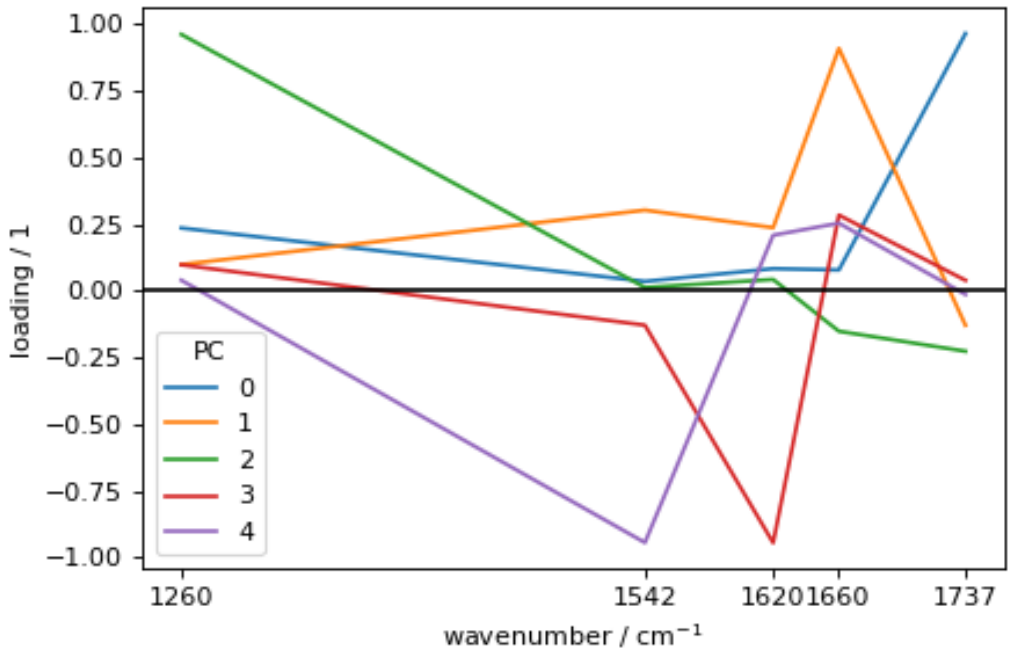

Figure 3.25: Loadings plot of the principal components.

In the obtained spectra, see section 3.1.5, the dominant band is at 1737 cm^{-1}. Through PCA and AFM-IR imaging, it is possible to see that there is not only the carbonyl

Die approbierte gedruckte Originalversion dieser Diplomarbeit ist an der TU Wien Bibliothek verfügbar
The approved original version of this thesis is available in print at TU Wien Bibliothek.

band at 1737 cm^{-1} from the lipid bi-layer, but that the found EVs also have different chemical composition. It can be seen that PC0 has positive loadings at 1260 cm^{-1}, 1542 cm^{-1}, 1620 cm^{-1}, 1660 cm^{-1} and 1737 cm^{-1}. The more PC0 there is, the thicker the EV is at that pixel. PC1 has also positive loadings at 1260 cm^{-1}, 1542 cm^{-1}, 1620 cm^{-1}, 1737 cm^{-1}, but especially at 1660 cm^{-1}, which means that this pixel has has a stronger contribution from the bands associated with amide I. PC2 correlates positively at 1260 cm^{-1}, 1542 cm^{-1}, 1620 cm^{-1} and negatively at 1660 cm^{-1} and 1737 cm^{-1}. The loadings with opposing sings (1620 cm^{-1} and 1660 cm^{-1}) could indicate a difference in the secondary structure.

The scores plot to visualize the clusters in the data set is shown figure 3.26. Abstract rendering [60] was used again to avoid overprinting in denser areas.

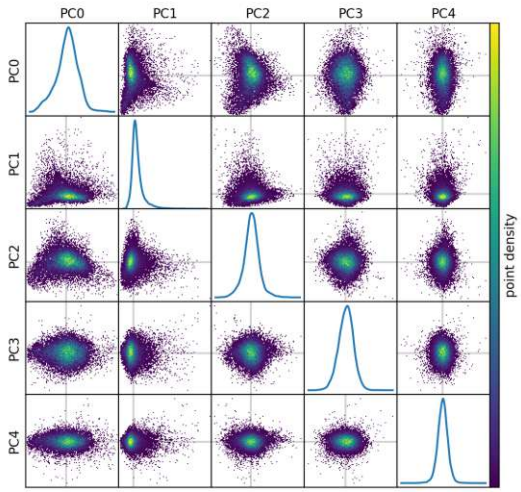

Figure 3.26: Scores plot of PC0 to PC4. Labels on the sides of the plot indicate the plotted scores. Along the diagonal the distribution of each score is depicted as density function. Grey lines indicate scores 0.

In comparison to the second measurement, where only PCO showed spreading in the data points (see 3.19), here, different dense areas can be seen in a lot of plots. In PC0 - PC1 a correlation can be seen, as the data points spread out in all directions, thus

Die approbierte gedruckte Originalversion dieser Diplomarbeit ist an der TU Wien Bibliothek verfügbar
The approved original version of this thesis is available in print at TU Wien Bibliothek.
TU Bibliothek Your knowledge hub WIEN

indicating different pixel have similarities and can be distinguished from each other. PC1 - PC2 shows also a spreading of the data points. This can be used to find differences in the protein structure.

By visualizing the PC in the found plots, the different composition can be seen (see figure 3.27).

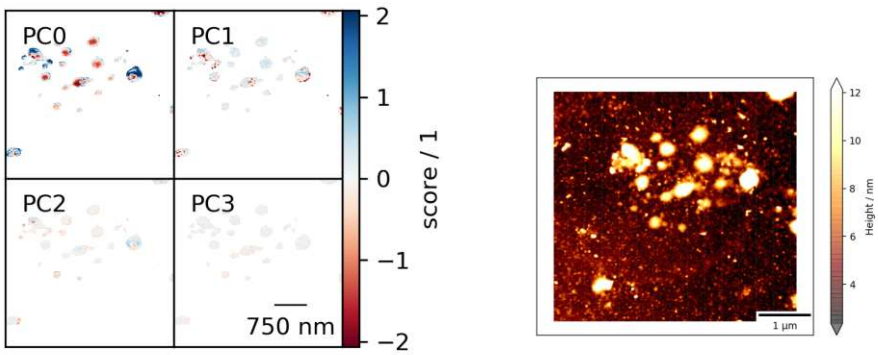

(a) Score Plot (b) Topography image

Figure 3.27: (a) Score plots applied onto the pixels. Every PC shows up at different pixels, thus underlining the difference in the vesicles. Positive (blue) and negative (red) scores can be seen. (b) topography image of the same area.

In each vesicle, a different PC has a high value, thus implying a different chemical composition. Most of the shown vesicle have both a very high (blue) and very low (red) values for PC0. This means they have areas with very high lipid content (blue, positive PC0). PC1 and PC2 compensate some of the red areas from PC0. This mean that there areas with high protein content (blue, positive PC1 and PC2). The differences between PC1 and PC2 in blue areas can be used to distinguish between protein structures. However, interpretation of these images is not straight forward, as already mentioned, and other chemometric methods could be advantageous.

As a last step the vesicle size was investigated. In figure 3.28 this can be seen.

It can be seen that there is slight upward trend in all wavenumbers, especially at

Die approbierte gedruckte Originalversion dieser Diplomarbeit ist an der TU Wien Bibliothek verfügbar
The approved original version of this thesis is available in print at TU Wien Bibliothek.
TU Bibliothek Your knowledge hub WIEN

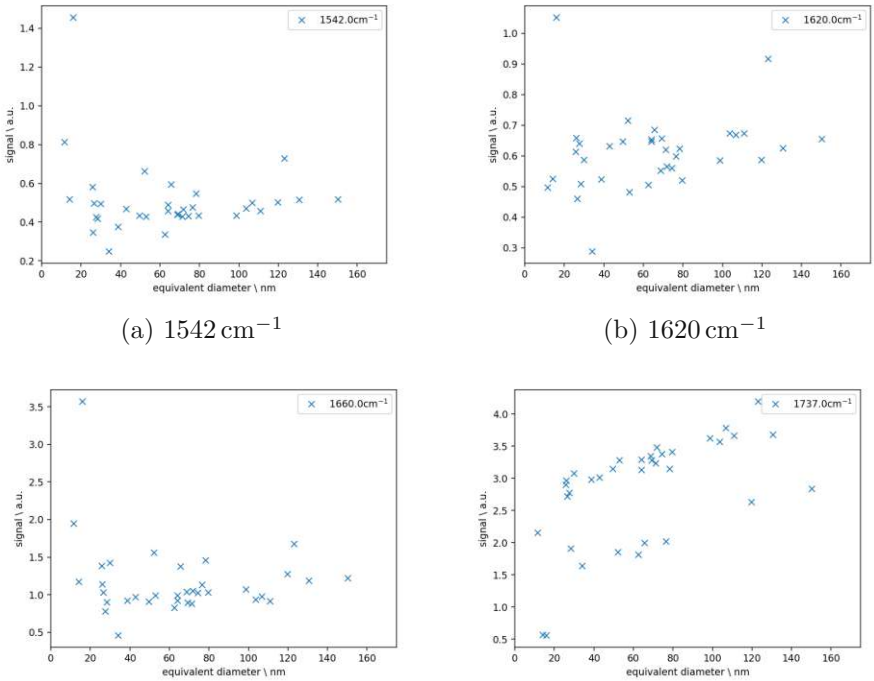

(a) $1542\,\mathrm{cm}^{-1}$ (b) $1620\,\mathrm{cm}^{-1}$

(c) $1660\,\mathrm{cm}^{-1}$ (d) $1737\,\mathrm{cm}^{-1}$

Figure 3.28: Equivalent diameter plotted against the signal at the respective wavenumber (a) $1542\,\mathrm{cm}^{-1}$ (b) $1620\,\mathrm{cm}^{-1}$ (c) $1660\,\mathrm{cm}^{-1}$ (d) $1737\,\mathrm{cm}^{-1}$. In all of the plots a positive trend is visible, especially at the (d) plot.

$1737\,\mathrm{cm}^{-1}$. The bigger the vesicle, the higher the signal gets. This would make sense, since bigger vesicles would mean more (protein, etc.,) can be stored inside of it.

3.3 Possible Sources of Error and Possibilities for Improvement

Although all in all, the chemical analysis of the vesicle worked out very well, there are still some possible errors in the whole procedure.

First and foremost, the technical handling of the experimental protocol (see chapter 2) is a significant source of error. As seen in section 3.1.4, it is possible that the microcontact

Die approbierte gedruckte Originalversion dieser Diplomarbeit ist an der TU Wien Bibliothek verfügbar
The approved original version of this thesis is available in print at TU Wien Bibliothek.
TU Bibliothek Your knowledge hub WIEN

printing does not work sometimes, and thus it is not possible to perform the chemical analysis. One possible reason for this failure is that the substrate was not clean enough for the AnteoBind™ Biosensor to bond onto the surface.

Furthermore, the dilution of the sample needs to be precisely adjusted, since an undiluted sample can lead to overloading (see figure 3.7), but a dilution that is too high can lead to vesicles no longer being able to be found. Both of these issues can be detected quickly during the measurement. However, at that point, they can not be corrected for anymore. Success of microcontact printing can also be verified before incubation with EVs via AFM. While not done for the samples analysed in this work, NTA could be be used to verify the EV concentration before incubation and the sample could then be diluted accordingly.

Incubation and sample preparation could introduce bias in sampling: our protocol does not verify that all, or even a representative fraction of EVs, have been captured on the substrate. The incubation time was derived from considerations about diffusion lengths. If the incubation time was selected too short, then large EVs would be underrepresented in our analysis. The CD9 anti-gen used to capture EVs in our protocol is typically understood to be an EV "marker", hence it should be present on all EVs. Nevertheless, vesicles without this anti-gen will not be captured in our protocol.

For some samples, the AFM-IR signals were barely above the noise level. In these cases, a higher laser power can help somewhat. However, if the laser power is set too high, the heat deposited in the vesicles can be high enough to destroy them. If this happens, it is not possible to get an IR signal from the same location again. In tapping-mode AFM-IR, other experimental parameters (drive strength, set-point, pulse length) and cantilever to cantilever variations can also affect the AFM-IR signal strength. Hence, these parameters should also be optimized if the signal is not high enough.

Die approbierte gedruckte Originalversion dieser Diplomarbeit ist an der TU Wien Bibliothek verfügbar
The approved original version of this thesis is available in print at TU Wien Bibliothek.
TU Bibliothek Your knowledge hub WIEN

Data evaluation can introduce some bias in the results. Both, LDA and segmentation require user input to detect vesicles. While the performance of the segmentation was spot-checked against a few vesicles and no obvious errors were found, errors that were present in segmentation, would have manifested in one of these ways:

1. *pixels on substrate around vesicles segmented as EV*: in this case, vesicles appear larger than they actually are. The average spectra per vesicle in this case also contains some contribution from the substrate. This would affect smaller vesicles more strongly.

2. *some pixels at the edge of vesicles not segmented as EV*: vesicles appear smaller. If they are laterally inhomogeneous, whichever component is found on the side will be underrepresented. It is not clear, whether this would affect smaller or larger vesicles more strongly, as it depends on the specific distribution of EV components within the EV.

3. *some (small) EVs not found*: pixels close to the hyperplane in LDA will have a low prediction probability. Our algorithm will still segment them as EV/substrate, if neighbouring pixels are segmented as EV/substrate. However, if not a single pixel in an EV is classified as "EV" with a high enough prediction probability, the whole EV will not be detected in the end. This likely affects very small EVs the most.

4. *EVs merged*: The watershed algorithm assumes that two EVs are always separated by substrate. If that is not the case, it could merge neighbouring EVs into a single, larger one. Merged EVs would show up as large vesicle with the chemical composition of a smaller one in our analysis.

Another big improvement point is the incubation time (see section 2.2.4). The 52 hours could be greatly shortened by using microfluidics. The same sample volume could be

Die approbierte gedruckte Originalversion dieser Diplomarbeit ist an der TU Wien Bibliothek verfügbar
The approved original version of this thesis is available in print at TU Wien Bibliothek.
TU Bibliothek Your knowledge hub WIEN

flushed over the printed pattern in a shorter amount of time. By doing this, the diffusion is not an issue anymore.

Die approbierte gedruckte Originalversion dieser Diplomarbeit ist an der TU Wien Bibliothek verfügbar
The approved original version of this thesis is available in print at TU Wien Bibliothek.
TU Bibliothek Your knowledge hub WIEN

CHAPTER 4

Conclusion

4.1 Conclusion

The aim of this thesis was to find a method to obtain label-free chemical information from single extracellular vesicles. The developed immobilization protocol is able to selectively deposit EVs on an AFM-IR compatible substrate via an anti-CD9 antibody. Nanoscale spatial resolution AFM-IR spectra of EVs compare well to FTIR bulk reference spectra, see chapter 3. For high throughput measurements of many EVs, hyperspectral images were assembled from many tapping mode AFM-IR images. Image segmentation was employed to find all pixels belonging to the same vesicles. This enabled us to study relationships between size and composition of EVs within different (sub-)populations of vesicles.

Die approbierte gedruckte Originalversion dieser Diplomarbeit ist an der TU Wien Bibliothek verfügbar
The approved original version of this thesis is available in print at TU Wien Bibliothek.
TU WIEN Bibliothek Your knowledge hub

Die approbierte gedruckte Originalversion dieser Diplomarbeit ist an der TU Wien Bibliothek verfügbar
The approved original version of this thesis is available in print at TU Wien Bibliothek.

List of Figures

1.1 Simplified force-distance curve [20] showing the course of the tip during contact mode. On the right, the probe bending is illustrated. 7

1.2 Operating regime of tapping mode [20]. The AFM probe oscillates back and forth between the repulsive and attractive regimes, losing contact completely in each cycle. On the right the bending of the cantilever is shown. 8

1.3 Principle of µCP 11

1.4 Schematic representation of a antibody 12

2.1 Plasma cleaning removes of organic compounds on the substrate and creates OH groups on the substrate. 17

2.2 Scheme of the steps to µCP the silicon substrate 18

2.3 Used stamp for the microcontact printing. 19

2.4 AFM phase image of the stamped pattern on the silicon surface 19

2.5 Backfilling the pattern with 100 µL BSA in PBS 20

2.6 Anti-CD9 antibodies holding the exosomes from the human milk 20

2.7 AFM image of the first incubated silicon with sample 21

2.8 Image of the used incubation chambers 22

2.9 width=0.6 23

2.10 AFM-IR phase image of the first sample, with the visible stamped pattern (marked with red circles) 23

Die approbierte gedruckte Originalversion dieser Diplomarbeit ist an der TU Wien Bibliothek verfügbar
The approved original version of this thesis is available in print at TU Wien Bibliothek.
TU Bibliothek Your knowledge hub WIEN

2.11 (a) phase image of the focused circle (b) height image of the focused circle 24
2.12 IR spectra comparison of the first found exosome. The bulk IR data (red line) matches the AFM-IR data (blue line) at the significant wavenumbers, see [15] 25
2.13 First iteration of the AFM-IR imaging with the respective wavenumbers (a) $1392\,\mathrm{cm}^{-1}$ (b) $1451\,\mathrm{cm}^{-1}$ (c) $1535\,\mathrm{cm}^{-1}$ and (d) $1660\,\mathrm{cm}^{-1}$ 25
2.14 (a) Two height images with a clear deviation from each other (b) The same height images after PCC was carried out, thus they are aligned in the same way 29
2.15 Two groups, with assigned features, which are being separated by the calculated hyperplane. 30
2.16 (a) Two-dimensional dataset with two features visualized. Most of the variance lies in one direction (marked as PC1) and describes the majority of the data. The second principal component (marked as PC2) lies orthogonal to PC1. (b) PC score plot of the dataset with the principal components as axis. Useful for clustering of the data along the selected principal components. 31
2.17 Height image after preprocessing, stacking and averaging 33
2.18 Identified areas on a topography image by the user, which are associated to "EVs" (blue) and "non-EVs" (orange). The chosen data is used as training data for the LDA. 34
2.19 Data after the LDA distinguishes between "EV" and "non-EV" by using "phase" and "height" as variables 36
2.20 Calculated hyperplane of the sample data, small overlaps of 'EV' into 'non-EV' are visible 36
2.21 Predicted EVs in the data by the LDA classifier 37
2.22 Comparison of the different LDA models 38
2.23 Plot of the AFM-IR signal at $1260\,\mathrm{cm}^{-1}$ only on pixels that are on an EV, as found by segmentation. 39

Die approbierte gedruckte Originalversion dieser Diplomarbeit ist an der TU Wien Bibliothek verfügbar
The approved original version of this thesis is available in print at TU Wien Bibliothek.
TU Bibliothek Your knowledge hub WIEN

2.24 Plot of the size comparison 42

3.1 (a) Location where the tip was (b) AFM-IR and IR spectra comparison . 44

3.2 Comparison of the IR measurement (red) with AFM-IR spectrum on the vesicle (dark blue) and next to the vesicle (light blue). The found vesicle (dark blue) has the same bands as the IR measurement (red), in contrast to the measurement next to the vesicle (blue). 45

3.3 All spectra taken from the second measurement 46

3.4 AFM-IR spectrum taken on a vesicle showing weak bands corresponding to the vesicle. (a) Location where the tip was (b) AFM-IR and IR spectra comparison 47

3.5 AFM-IR spectrum taken to the side of a vesicle showing only bands assigned to the substrate and the AFM tip. (a) Location where the tip was (b) AFM-IR and IR spectra comparison 47

3.6 A spectrum taken on a vesicle. The spectrum has a high noise level but nevertheless bands assigned to the vesicle can be made out. (a) Location where the tip was (b) AFM-IR and IR spectra comparison 48

3.7 Phase image with a overload of vesicles 48

3.8 Phase images from the 50:1 diluted sample showing no printed circles . . 49

3.9 Overview of all AFM-IR spectra taken on the sample incubated with a 1:10 diluted vesicle suspension. 50

3.10 (a) Location where the tip was (b) AFM-IR and IR spectra comparison . 50

3.11 AFM-IR spectrum showing high bands assigned to lipids and low (or no) contributions from proteins. (a) Location where the tip was (b) AFM-IR and IR spectra comparison 51

Die approbierte gedruckte Originalversion dieser Diplomarbeit ist an der TU Wien Bibliothek verfügbar
The approved original version of this thesis is available in print at TU Wien Bibliothek.
TU Bibliothek Your knowledge hub WIEN

3.12 AFM-IR spectra taken on the same vesicle with slightly different positions. The first spectrum (b) is dominated by lipid bands, while in the second spectrum (d) amide bands are clearly visible. Location of the tip (a), (c) and their respective spectra (b), (d) 52

3.13 AFM-IR images of the second vesicle sample (1:2 dilution, see also section 3.1.3 for spectra and topography images) with the respective wavenumbers (a) 1392 cm^{-1} (b) 1451 cm^{-1} (c) 1535 cm^{-1} (d) 1660 cm^{-1} (e) 1737 cm^{-1} (f) 1097 cm^{-1} 54

3.14 AFM-IR images of the sample incubated with 1:10 diluted vesicle suspension. Imaging was carried out the following (a) 1542 cm^{-1} (b) 1620 cm^{-1} (c) 1660 cm^{-1} and (d) 1737 cm^{-1} 55

3.15 Mask used for training the LDA. (a) Mask plotted on top the height image and on top of the (b) phase image with marked "EVs" (red) and "non-EVs" (yellow) 56

3.16 Comparison of the different LDA approaches 57

3.17 Plots of the found EVs at the respective wavenumber **(a)** 1392 cm^{-1} **(b)** 1451 cm^{-1} **(c)** 1542 cm^{-1} **(d)** 1660 cm^{-1} **(e)** 1737 cm^{-1} 57

3.18 Loadings plot relating principal components to wavenumbers. 59

3.19 Scores plot of PC0 to PC3. Labels on the sides of the plot indicate the plotted scores. Along the diagonal the distribution of each score is depicted as density function. Grey lines indicate scores of 0. 60

3.20 (a) Score plots applied onto the pixels. Every PC shows up at different pixels, thus underlining the difference in the vesicles. Positive (blue) and negative (red) scores can be seen. (b) topography image of the same area. 61

Die approbierte gedruckte Originalversion dieser Diplomarbeit ist an der TU Wien Bibliothek verfügbar
The approved original version of this thesis is available in print at TU Wien Bibliothek.
TU Bibliothek Your knowledge hub WIEN

3.21 Equivalent diameter plotted against the signal at the respective wavenumbers (a) 1392 cm^{-1} (b) 1542 cm^{-1} (c) 1660 cm^{-1} (d) 1737 cm^{-1}. In all of the plots a positive trend is visible. Note that the very large vesicle was excluded in this diagram. 62
3.22 (a) Mask on the height image and on the (b) phase image with marked "EVs" (red) and "non-EVs" (yellow) 62
3.23 Comparison of the different LDA approaches 63
3.24 Plots of the found EVs at the respective wavenumbers (a) 1542 cm^{-1} (b) 1620 cm^{-1} (c) 1660 cm^{-1} and (d) 1737 cm^{-1} 63
3.25 Loadings plot of the principal components. 64
3.26 Scores plot of PC0 to PC4. Labels on the sides of the plot indicate the plotted scores. Along the diagonal the distribution of each score is depicted as density function. Grey lines indicate scores 0. 65
3.27 (a) Score plots applied onto the pixels. Every PC shows up at different pixels, thus underlining the difference in the vesicles. Positive (blue) and negative (red) scores can be seen. (b) topography image of the same area. 66
3.28 Equivalent diameter plotted against the signal at the respective wavenumber (a) 1542 cm^{-1} (b) 1620 cm^{-1} (c) 1660 cm^{-1} (d) 1737 cm^{-1}. In all of the plots a positive trend is visible, especially at the (d) plot. 67

Die approbierte gedruckte Originalversion dieser Diplomarbeit ist an der TU Wien Bibliothek verfügbar
The approved original version of this thesis is available in print at TU Wien Bibliothek.
TU Bibliothek Your knowledge hub WIEN

Die approbierte gedruckte Originalversion dieser Diplomarbeit ist an der TU Wien Bibliothek verfügbar
The approved original version of this thesis is available in print at TU Wien Bibliothek.

List of Tables

2.1 List of the various python libraries and their functions 27

2.2 Example dataframe. The particle mask distinguishes between "EVs", labelled as 1.0, and "non-EVs", labelled as 2.0. 35

3.1 Wavenumbers used for AFM-IR imaging 53

3.2 Explained variance for the individual principle components in the second measurement. 58

3.3 Explained variance for the individual principle components in the second measurement 64

Die approbierte gedruckte Originalversion dieser Diplomarbeit ist an der TU Wien Bibliothek verfügbar
The approved original version of this thesis is available in print at TU Wien Bibliothek.
TU WIEN Bibliothek Your knowledge hub

Die approbierte gedruckte Originalversion dieser Diplomarbeit ist an der TU Wien Bibliothek verfügbar
The approved original version of this thesis is available in print at TU Wien Bibliothek.

List of Algorithms

Code Listing 4.1: Loading the data

```
anafile = apt.read(("29072022_1zu10_overnight.axz"))

def rename_if_exists(renames):
    def renamer(ds):
        used_dict = {}
        for k,v in renames.items():
            if k in ds:
                used_dict[k] = v
        return ds.rename(used_dict)
    return renamer

rename = rename_if_exists({"//ZI/*/DEMODS/2/R":"TapIR"})
datasets = [rename(imagelist_to_Dataset(imglst)) for imglst in
                                        get_concurrent_images(anafile.
                                        HeightMaps.values()).values()]
datasets_dict = {ds.Label:ds for ds in datasets}

#picking the right 'Height {} (PrimaryTrace)'
verwendet = ['Height {} (PrimaryTrace)'.format(idx) for idx in [8,9,10,11,12]
                                        ]

#looking through the wavenumbers
[datasets_dict[k].IRWavenumber for k in verwendet]
```


Die approbierte gedruckte Originalversion dieser Diplomarbeit ist an der TU Wien Bibliothek verfügbar
The approved original version of this thesis is available in print at TU Wien Bibliothek.
TU Bibliothek Your knowledge hub WIEN

```
#checking the shape
[datasets_dict[k].height.shape for k in verwendet]

def nanquantile_correct(arr, dim="x"):
    return xr.apply_ufunc(lambda x: x - np.nanquantile(x, .01),arr,
                                          input_core_dims=[[dim]],
                                          output_core_dims=[[dim]],vectorize
                                          =True)

for ds in [datasets_dict[k] for k in verwendet]:
    ds["height"] = nanquantile_correct(ds.height)
```

Code Listing 4.2: Performing PCC

```
#performing the phase cross correlation
homo = Homography_PCC(datasets_dict[verwendet[0]], "height")
for ds in [datasets_dict[k] for k in verwendet]:
    ds.homography["shift"] = homo.find_homography(ds, "height")

def float_with_unit(x):
    return  float(x.split(" ")[0])

attrs_to_coords = {"IRWavenumber": float_with_unit,
                   "IRAttenuation": float_with_unit,
                   "Setpoint": float_with_unit,
                   "ACDriveFrequency":float_with_unit}

def stack_ds(datasets, homography,new_dim, attrs, attrs_to_coords):
    def none_to_lambda(lam):
        if lam is None:
            return lambda x: x
        else:
            return lam
```


Die approbierte gedruckte Originalversion dieser Diplomarbeit ist an der TU Wien Bibliothek verfügbar
The approved original version of this thesis is available in print at TU Wien Bibliothek.
TU Bibliothek Your knowledge hub WIEN

```
    new_coords = {attr:[none_to_lambda(fun)(ds.attrs[attr]) for ds in
                                        datasets] for attr, fun in
                                        attrs_to_coords.items()}
    ds = xr.concat([ds.homography.project_dataset(homography=homography) for
                                        ds in datasets],
                    combine_attrs="drop",
                    coords="all",
                    join="outer",
                    dim=new_dim)
    ds.attrs = attrs
    for name, vals in new_coords.items():
        ds.coords[name] = (new_dim, vals)
    return ds

[datasets_dict[k] for k in verwendet][1].homography.project_dataset("shift").
                                        coords["y"]

stacked = stack_ds([datasets_dict[k] for k in verwendet], "shift", "
                                        wavenumber",attrs=datasets_dict[
                                        verwendet[0]].attrs,  attrs_to_coords=
                                        attrs_to_coords)
stacked = stacked.set_index(wavenumber="IRWavenumber")
stacked_coords = stacked.transpose("y","x",...).homography.with_coords("pos")
[datasets_dict[k] for k in verwendet][-1].homography["shift"]
[datasets_dict[k] for k in verwendet][0].homography.project_dataset("shift",)
                                        .dropna("y","all").dropna("x","all").
                                        coords["y"]

stacked_selected = stacked_coords.sortby("wavenumber").isel({"wavenumber":
                                        slice(0,7)})
```

Code Listing 4.3: Python code for the correction of the data

```
def plane(x, k1, k2, o):
```


Die approbierte gedruckte Originalversion dieser Diplomarbeit ist an der TU Wien Bibliothek verfügbar
The approved original version of this thesis is available in print at TU Wien Bibliothek.
TU Bibliothek Your knowledge hub WIEN

```
    return  o +k1*x[0]+ k2*x[1]

height = stacked_selected.height.mean("wavenumber", skipna=False)
height = height - plane([height.x, height.y],*height.curvefit(["x", "y"],
                                        plane).curvefit_coefficients.values)
height = height - xr.apply_ufunc(np.nanquantile, height, kwargs={"q":.1},
                                        input_core_dims=[["x"]],
                                        output_core_dims=[[]], vectorize=True)
height = height - np.min(height)

phase = stacked_selected.phase1.mean("wavenumber", skipna=False)
```

Code Listing 4.4: Image segmenter for the LDA

```
from mpl_interactions import image_segmenter
import ipywidgets as widgets

#choose your data for the LDA
#group 1: EVs
#group 2: non-EVs

N_classes = 2
class_selector = widgets.Dropdown(options=list(range(1, N_classes + 1)),
                                        description="class")



def update(change):
    multi_class_segmenter.current_class = class_selector.value
    multi_class_segmenter.erasing = erasing_button.value

erasing_button = widgets.Checkbox(value=False, description="Erasing")
erasing_button.observe(update, names="value")

class_selector.observe(update, names="value")
```


Die approbierte gedruckte Originalversion dieser Diplomarbeit ist an der TU Wien Bibliothek verfügbar
The approved original version of this thesis is available in print at TU Wien Bibliothek.
TU Bibliothek Your knowledge hub WIEN

```
multi_class_segmenter = image_segmenter(phase, nclasses=2, mask_alpha=0.76,
                                        mask=np.load("maske.npy"))
display(widgets.HBox([erasing_button, class_selector]))
display(multi_class_segmenter)
```

Code Listing 4.5: Creation of the data frame

```
np.save("maske",multi_class_segmenter.mask)


mask = np.load("maske.npy")
mask.shape


height_phase = xr.Dataset({"height":height, "phase":phase, "particle_mask":((
                                        "y","x"),multi_class_segmenter.mask)})
df_hp = height_phase[["height", "phase", "particle_mask"]].stack(pos={"x","y"
                                        }).to_pandas().drop("Xpos",1).drop("
                                        Ypos",1)
df_hp = df_hp.loc[df_hp.particle_mask!=0].reset_index(drop=True)
```

Code Listing 4.6: Python code for the LDA

```
import autosklearn.classification
import sklearn.model_selection
import sklearn.datasets
import sklearn.metrics
from sklearn.preprocessing import LabelEncoder
from sklearn.discriminant_analysis import LinearDiscriminantAnalysis,
                                        QuadraticDiscriminantAnalysis


data = df_hp.values
X, y = data[:, :-1], data[:, -1]
X = X.astype('float32')
y = y
X_train, X_test, y_train, y_test = sklearn.model_selection.train_test_split(X
                                        , y, random_state=1)
```


Die approbierte gedruckte Originalversion dieser Diplomarbeit ist an der TU Wien Bibliothek verfügbar
The approved original version of this thesis is available in print at TU Wien Bibliothek.
TU Bibliothek Your knowledge hub WIEN

```
lda = LinearDiscriminantAnalysis()
lda.fit(X_train, y_train)
y_hat = lda.predict(X_test)
print("Accuracy score", sklearn.metrics.accuracy_score(y_test, y_hat))

plt.figure()
print(X)
sc = plt.scatter(X[:,0], X[:,1], c= y)
plt.colorbar(sc)
plt.xlabel("height / nm")
plt.ylabel("phase / deg")
```

Code Listing 4.7: Creation of the hyperlane

```
df_hp_all = height_phase[["height", "phase"]].stack(pos={"x","y"}).to_pandas
                                        ().drop("Xpos",1).drop("Ypos",1)
X_pred =  df_hp_all.values
nan_mask = np.logical_or(np.isnan(X_pred)[:,0],np.isnan(X_pred)[:,1])
y_pred = lda.predict(X_pred[~nan_mask])
output = np.nan * np.zeros(X_pred.shape[0])
output[~nan_mask] = y_pred

df_hp_all["y_pred"] = output

from sklearn.inspection import DecisionBoundaryDisplay

fig, ax = plt.subplots()
disp = DecisionBoundaryDisplay.from_estimator(lda, X_pred[~nan_mask],
                                        response_method="predict_proba",
                                        plot_method="pcolormesh", ax=ax)
plt.colorbar(disp.surface_)
sc = ax.scatter(X_pred[~nan_mask][:,0], X_pred[~nan_mask][:,1], c= np.where(
                                        y_pred==1, "r", "k"), marker="x")
```


Die approbierte gedruckte Originalversion dieser Diplomarbeit ist an der TU Wien Bibliothek verfügbar
The approved original version of this thesis is available in print at TU Wien Bibliothek.
TU Bibliothek Your knowledge hub WIEN

```
plt.xlabel("height / nm")
plt.ylabel("phase / deg")
```

Code Listing 4.8: Comparison of the LDA

```
#plots for the enhanced LDA
import matplotlib.pyplot as plt
from matplotlib.gridspec import GridSpec

from sklearn.calibration import CalibratedClassifierCV, CalibrationDisplay
from sklearn.linear_model import LogisticRegression
from sklearn.naive_bayes import GaussianNB

lr = LogisticRegression(C=1.0)
lda = LinearDiscriminantAnalysis()
lda_isotonic = CalibratedClassifierCV(lda, cv=2, method="isotonic")
lda_sigmoid = CalibratedClassifierCV(lda, cv=2, method="sigmoid")

lda_list = [
    (lr, "Logistic"),
    (lda, "LDA"),
    (lda_isotonic, "LDA + Isotonic"),
    (lda_sigmoid, "LDA + Sigmoid"),
]

fig = plt.figure(figsize=(10, 10))
gs = GridSpec(4, 2)
colors = plt.cm.get_cmap("Dark2")

ax_calibration_curve = fig.add_subplot(gs[:2, :2])
calibration_displays = {}
for i, (lda, name) in enumerate(lda_list):
    lda.fit(X_train, y_train)
    display = CalibrationDisplay.from_estimator(
```


Die approbierte gedruckte Originalversion dieser Diplomarbeit ist an der TU Wien Bibliothek verfügbar
The approved original version of this thesis is available in print at TU Wien Bibliothek.
TU WIEN Bibliothek Your knowledge hub

```
        lda,
        X_test,
        y_test,
        n_bins=10,
        name=name,
        ax=ax_calibration_curve,
        color=colors(i),
    )
    calibration_displays[name] = display

ax_calibration_curve.grid()
ax_calibration_curve.set_title("Calibration plots (LDA)")

# Add histogram
grid_positions = [(2, 0), (2, 1), (3, 0), (3, 1)]
for i, (_, name) in enumerate(lda_list):
    row, col = grid_positions[i]
    ax = fig.add_subplot(gs[row, col])

    ax.hist(
        calibration_displays[name].y_prob,
        range=(0, 1),
        bins=10,
        label=name,
        color=colors(i),
    )
    ax.set(title=name, xlabel="Mean predicted probability", ylabel="Count")

plt.tight_layout()
plt.show()
```

Code Listing 4.9: Python code for the final data frame

Die approbierte gedruckte Originalversion dieser Diplomarbeit ist an der TU Wien Bibliothek verfügbar
The approved original version of this thesis is available in print at TU Wien Bibliothek.
TU Bibliothek Your knowledge hub WIEN

```
df_hp_all = height_phase[["height", "phase"]].stack(pos={"x","y"}).to_pandas
                                        ().drop("Xpos",1).drop("Ypos",1)
X_pred =  df_hp_all.values
nan_mask = np.logical_or(np.isnan(X_pred)[:,0],np.isnan(X_pred)[:,1])
y_pred = lda.predict(X_pred[~nan_mask])
output = np.nan * np.zeros(X_pred.shape[0])
output[~nan_mask] = y_pred
df_hp_all["y_pred"] = output

df_hp_all_dropna = df_hp_all.dropna().drop(columns=['y_pred'])
X_pred_dropna = df_hp_all_dropna.values
nan_mask = np.logical_or(np.isnan(X_pred_dropna)[:,0],np.isnan(X_pred_dropna)
                                        [:,1])
y_pred_dropna = lda_sigmoid.predict_proba(X_pred_dropna[~nan_mask])
output1 = np.nan * np.zeros(X_pred_dropna.shape[0])
output2 = output1.copy()
output1[~nan_mask] = y_pred_dropna[:,0]
output2[~nan_mask] = y_pred_dropna[:,1]



df_hp_all_dropna["proba_cl1"] = output1
df_hp_all_dropna["proba_cl2"] = output2
```

Code Listing 4.10: Python code for the segmentation

```
data = df_hp_all_dropna.values
vesikel = xr.Dataset.from_dataframe(df_hp_all_dropna).transpose("y",...)
edges = filters.sobel(vesikel['height'])

#segmentation

markers = np.zeros_like(vesikel['height'])
foreground, background = 1, 2
markers[ (vesikel['proba_cl2']>.1)]  = background
```


Die approbierte gedruckte Originalversion dieser Diplomarbeit ist an der TU Wien Bibliothek verfügbar
The approved original version of this thesis is available in print at TU Wien Bibliothek.
TU Bibliothek Your knowledge hub WIEN

```
markers[(vesikel['proba_cl1']>.95) ] = foreground

ws = watershed(edges, markers)
seg1 = label(ws == foreground, )

expanded = expand_labels(seg1, distance=1)
```

Code Listing 4.11: Preparing data for PCA

```
~(expanded==0)
expanded_da = xr.DataArray(expanded, dims = vesikel.dims, coords = vesikel.
                                        coords)
stacked_selected.TapIR.reindex_like(expanded_da).where(expanded_da==1)
spectra_per_pixel = stacked_selected.TapIR.reindex_like(expanded_da).where(
                                        expanded_da!=0).stack(sample=("x","y")
                                        ).dropna("sample")
x = spectra_per_pixel.unstack("sample").sortby("y").sortby("x").x
y = spectra_per_pixel.unstack("sample").sortby("y").sortby("x").y
spectra_per_pixel.unstack("sample").sortby("y").sortby("x")\
.reindex({"x":np.arange(x.min(), x.max(), 1), "y":np.arange(y.min(), y.max(),
                                        1)})\
.hvplot.quadmesh(x="x", y="y", rasterize=True, grid=True)
```

Code Listing 4.12: Python code for the PCA

```
scores.unstack("sample").sortby("x").sortby("y")\
.reindex({"x":np.arange(x.min(), x.max(), 1), "y":np.arange(y.min(), y.max(),
                                        1)})\
.hvplot.quadmesh(x="x", y="y", rasterize=True, grid=True)

from sklearn.decomposition import PCA
from sklearn.preprocessing import Normalizer
from sklearn.pipeline import make_pipeline

n_components = 5
```


Die approbierte gedruckte Originalversion dieser Diplomarbeit ist an der TU Wien Bibliothek verfügbar
The approved original version of this thesis is available in print at TU Wien Bibliothek.
TU Bibliothek Your knowledge hub WIEN

```
pca_norm = make_pipeline(wrap(Normalizer(), sample_dim="sample"), wrap(PCA(
                                        n_components=n_components), reshapes="
                                        wavenumber", sample_dim="sample"))

pca_norm.fit(X)
scores = pca_norm.transform(X).rename(wavenumber="PC").assign_coords(PC=np.
                                        arange(n_components))

components = like_xr(pca_norm.steps[-1][1].components_, spectra_per_pixel, "
                                        wavenumber", "PC", transpose=True).
                                        assign_coords(PC=np.arange(
                                        n_components)).sortby("wavenumber")

plt.figure()
components.plot.line(x="wavenumber");

df = scores.T.to_pandas().reset_index(drop=True)

df.set_axis([str(c) for c in df.columns], axis="columns", inplace=True)

x_scale = np.amax(np.abs(scores))

fig, ax = plt.subplots(n_components,n_components, figsize=(10,10), sharex=
                                        True, sharey=True)
for pc1, pc2 in product(range(n_components), range(n_components)):
    if pc1 == pc2:
        ax[pc1,pc2].get_shared_y_axes().remove(ax[pc1, pc2])
        sns.kdeplot(scores.sel(PC=pc2), ax=ax[pc1, pc2])

    else:
        dsshow(df, dsPoint(str(pc1), str(pc2)), ax=ax[pc1,pc2], x_range=[-
                                                x_scale, +x_scale], y_range=[-
```


Die approbierte gedruckte Originalversion dieser Diplomarbeit ist an der TU Wien Bibliothek verfügbar
The approved original version of this thesis is available in print at TU Wien Bibliothek.
TU Bibliothek Your knowledge hub WIEN

```
                                                x_scale, +x_scale])

scores.unstack("sample").sortby("x").sortby("y")\
.reindex({"x":np.arange(x.min(), x.max(), 1), "y":np.arange(y.min(), y.max(),
                                        1)})\
.hvplot.quadmesh(x="x", y="y", rasterize=True, grid=True)
```

Code Listing 4.13: Python code for the size distribution

```
group_height = height.reindex_like(expanded_da).groupby(expanded_da)
from scipy.interpolate import SmoothBivariateSpline, RectBivariateSpline

def integrate(gh, del_x, del_y):
    arr= gh.unstack("stacked_x_y").sortby("x").sortby("y")
    arr = arr.where(~np.isnan(arr), 0)
    interp = RectBivariateSpline(arr.x.to_numpy()*del_x, arr.y.to_numpy()*
                                        del_y, arr.to_numpy(), kx=1, ky=1,
                                         )
    return xr.DataArray(interp.integral(arr.x.min()*del_x, arr.x.max()*del_x,
                                        arr.y.min()*del_y, arr.y.max()*
                                        del_y))

vesicle_volume = group_height.map(integrate, args=(1000*height.Xpos.diff("x")
                                    .median().to_numpy(),1000*np.abs(
                                    height.Ypos.diff("y").median().
                                    to_numpy()))).isel(group=slice(1,None)
                                    )
spectra_volume = xr.Dataset({"spectra":vesicle_groups.mean(dim="sample"), "
                                    volume":vesicle_volume })
```


Die approbierte gedruckte Originalversion dieser Diplomarbeit ist an der TU Wien Bibliothek verfügbar
The approved original version of this thesis is available in print at TU Wien Bibliothek.
TU Bibliothek Your knowledge hub WIEN

Bibliography

[1] Kanchan Vaswani et al. "A Method for the Isolation of Exosomes from Human and Bovine Milk". In: *Journal of Nutrition and Metabolism* 2019 (Dec. 3, 2019), pp. 1–6. ISSN: 2090-0724, 2090-0732. DOI: 10.1155/2019/5764740.

[2] Eduard Willms et al. "Extracellular Vesicle Heterogeneity: Subpopulations, Isolation Techniques, and Diverse Functions in Cancer Progression". In: *Frontiers in Immunology* 9 (Apr. 30, 2018), p. 738. ISSN: 1664-3224. DOI: 10.3389/fimmu.2018.00738.

[3] Laura Doyle and Michael Wang. "Overview of Extracellular Vesicles, Their Origin, Composition, Purpose, and Methods for Exosome Isolation and Analysis". In: *Cells* 8.7 (July 15, 2019), p. 727. ISSN: 2073-4409. DOI: 10.3390/cells8070727.

[4] Michela Battistelli and Elisabetta Falcieri. "Apoptotic Bodies: Particular Extracellular Vesicles Involved in Intercellular Communication". In: *Biology* 9.1 (Jan. 20, 2020), p. 21. ISSN: 2079-7737. DOI: 10.3390/biology9010021.

[5] Sangiliyandi Gurunathan et al. "Review of the Isolation, Characterization, Biological Function, and Multifarious Therapeutic Approaches of Exosomes". In: *Cells* 8.4 (Apr. 3, 2019), p. 307. ISSN: 2073-4409. DOI: 10.3390/cells8040307.

Die approbierte gedruckte Originalversion dieser Diplomarbeit ist an der TU Wien Bibliothek verfügbar
The approved original version of this thesis is available in print at TU Wien Bibliothek.
TU Bibliothek Your knowledge hub WIEN

[6] María Yáñez-Mó et al. “Biological Properties of Extracellular Vesicles and Their Physiological Functions”. In: *Journal of Extracellular Vesicles* 4.1 (Jan. 1, 2015), p. 27066. ISSN: 2001-3078. DOI: 10.3402/jev.v4.27066.

[7] James Monypenny et al. “ALIX Regulates Tumor-Mediated Immunosuppression by Controlling EGFR Activity and PD-L1 Presentation”. In: *Cell Reports* 24.3 (July 2018), pp. 630–641. ISSN: 22111247. DOI: 10.1016/j.celrep.2018.06.066.

[8] R. Steven Conlan et al. “Exosomes as Reconfigurable Therapeutic Systems”. In: *Trends in Molecular Medicine* 23.7 (July 2017), pp. 636–650. ISSN: 14714914. DOI: 10.1016/j.molmed.2017.05.003.

[9] Michael B. Dinkins et al. “Exosome Reduction in Vivo Is Associated with Lower Amyloid Plaque Load in the 5XFAD Mouse Model of Alzheimer’s Disease”. In: *Neurobiology of Aging* 35.8 (Aug. 2014), pp. 1792–1800. ISSN: 01974580. DOI: 10.1016/j.neurobiolaging.2014.02.012.

[10] Valentina Palmieri et al. “Dynamic Light Scattering for the Characterization and Counting of Extracellular Vesicles: A Powerful Noninvasive Tool”. In: *Journal of Nanoparticle Research* 16.9 (Sept. 2014), p. 2583. ISSN: 1388-0764, 1572-896X. DOI: 10.1007/s11051-014-2583-z.

[11] Cicek Gercel-Taylor et al. “Nanoparticle Analysis of Circulating Cell-Derived Vesicles in Ovarian Cancer Patients”. In: *Analytical Biochemistry* 428.1 (Sept. 2012), pp. 44–53. ISSN: 00032697. DOI: 10.1016/j.ab.2012.06.004.

[12] Wei Zhang et al. “Characterization of Exosomes Derived from Ovarian Cancer Cells and Normal Ovarian Epithelial Cells by Nanoparticle Tracking Analysis”. In: *Tumor Biology* 37.3 (Mar. 2016), pp. 4213–4221. ISSN: 1010-4283, 1423-0380. DOI: 10.1007/s13277-015-4105-8.

Die approbierte gedruckte Originalversion dieser Diplomarbeit ist an der TU Wien Bibliothek verfügbar
The approved original version of this thesis is available in print at TU Wien Bibliothek.
TU Bibliothek Your knowledge hub WIEN

[13] Rafal Szatanek et al. “The Methods of Choice for Extracellular Vesicles (EVs) Characterization”. In: *International Journal of Molecular Sciences* 18.6 (May 29, 2017), p. 1153. ISSN: 1422-0067. DOI: 10.3390/ijms18061153.

[14] Sean Gallagher et al. “Immunoblotting and Immunodetection”. In: *Current Protocols in Cell Biology* 52.1 (2011), pp. 6.2.1–6.2.28. DOI: 10.1002/0471143030.cb0602s52.

[15] Victoria Ramos-Garcia et al. “ATR-FTIR Spectroscopy for the Routine Quality Control of Exosome Isolations”. In: *Chemometrics and Intelligent Laboratory Systems* 217 (Oct. 2021), p. 104401. ISSN: 01697439. DOI: 10.1016/j.chemolab.2021.104401.

[16] Zoltán Bacsik, János Mink, and Gábor Keresztury. “FTIR Spectroscopy of the Atmosphere. I. Principles and Methods”. In: *Applied Spectroscopy Reviews* 39.3 (Dec. 31, 2004), pp. 295–363. ISSN: 0570-4928, 1520-569X. DOI: 10.1081/ASR-200030192.

[17] Norman Sheppard. “The Historical Development of Experimental Techniques in Vibrational Spectroscopy”. In: *Handbook of Vibrational Spectroscopy*. Ed. by John M. Chalmers and Peter R. Griffiths. Chichester, UK: John Wiley & Sons, Ltd, Aug. 15, 2006, s0101. ISBN: 978-0-471-98847-2 978-0-470-02732-5. DOI: 10.1002/0470027320.s0101.

[18] Barbara Stuart. “Infrared Spectroscopy”. In: *Kirk-Othmer Encyclopedia of Chemical Technology*. John Wiley & Sons, Ltd, 2005. ISBN: 978-0-471-23896-6. DOI: 10.1002/0471238961.0914061810151405.a01.pub2.

[19] Peter R. Griffiths and James A. De Haseth. *Fourier Transform Infrared Spectrometry*. 2nd ed. Chemical Analysis v. 171. Hoboken, N.J: Wiley-Interscience, 2007. 529 pp. ISBN: 978-0-471-19404-0.

Die approbierte gedruckte Originalversion dieser Diplomarbeit ist an der TU Wien Bibliothek verfügbar
The approved original version of this thesis is available in print at TU Wien Bibliothek.
TU Bibliothek Your knowledge hub WIEN

[20] Georg Ramer. “Development and Characterization of a Near-Field Infrared Microscope by the Coupling of AFM and QCL Spectroscopy”. In: (2016).

[21] Andreas Schwaighofer and Bernhard Lendl. “Quantum Cascade Laser-Based Infrared Transmission Spectroscopy of Proteins in Solution”. In: *Vibrational Spectroscopy in Protein Research*. Elsevier, 2020, pp. 59–88. ISBN: 978-0-12-818610-7. DOI: 10.1016/B978-0-12-818610-7.00003-7.

[22] Peter Jonathan Eaton and Paul West. *Atomic Force Microscopy*. Oxford ; New York: Oxford University Press, 2010. 248 pp. ISBN: 978-0-19-957045-4 978-0-19-882628-6.

[23] R. Hoffmann et al. “Mechanical Manifestations of Rare Atomic Jumps in Dynamic Force Microscopy”. In: *Nanotechnology* 18.39 (Sept. 2007), p. 395503. DOI: 10.1088/0957-4484/18/39/395503.

[24] Neal Crampton et al. “Fast-Scan Atomic Force Microscopy Reveals That the Type III Restriction Enzyme EcoP15I Is Capable of DNA Translocation and Looping”. In: *Proceedings of the National Academy of Sciences* 104.31 (2007), pp. 12755–12760. DOI: 10.1073/pnas.0700483104.

[25] Q Zhong, K Kjoller, and V B Ehngs. “Fractured Polymer/Silica Fiber Surface Studied by Tapping Mode Atomic Force Microscopy”. In: (1993).

[26] R García. “Dynamic Atomic Force Microscopy Methods”. In: *Surface Science Reports* 47.6-8 (Sept. 2002), pp. 197–301. ISSN: 01675729. DOI: 10.1016/S0167-5729(02)00077-8.

[27] S. N. Magonov, V. Elings, and M.-H. Whangbo. “Phase Imaging and Stiffness in Tapping-Mode Atomic Force Microscopy”. In: *Surface Science* 375.2 (1997), pp. L385–L391. ISSN: 0039-6028. DOI: 10.1016/S0039-6028(96)01591-9.

[28] F. Tamburini et al. “Overcoming the Rayleigh Criterion Limit with Optical Vortices”. In: *Physical Review Letters* 97.16 (Oct. 16, 2006), p. 163903. ISSN: 0031-9007, 1079-7114. DOI: 10.1103/PhysRevLett.97.163903.

Die approbierte gedruckte Originalversion dieser Diplomarbeit ist an der TU Wien Bibliothek verfügbar
The approved original version of this thesis is available in print at TU Wien Bibliothek.
TU Bibliothek Your knowledge hub WIEN

[29] A. Dazzi et al. “Subwavelength Infrared Spectromicroscopy Using an AFM as a Local Absorption Sensor”. In: *Infrared Physics & Technology* 49.1-2 (Sept. 2006), pp. 113–121. ISSN: 13504495. DOI: 10.1016/j.infrared.2006.01.009.

[30] Jeffrey J. Schwartz, Devon S. Jakob, and Andrea Centrone. “A Guide to Nanoscale IR Spectroscopy: Resonance Enhanced Transduction in Contact and Tapping Mode AFM-IR”. In: *Chemical Society Reviews* 51.13 (2022), pp. 5248–5267. ISSN: 0306-0012, 1460-4744. DOI: 10.1039/D2CS00095D.

[31] Karin Wieland et al. “Nanoscale Chemical Imaging of Individual Chemotherapeutic Cytarabine-Loaded Liposomal Nanocarriers”. In: *Nano Research* 12.1 (Jan. 2019), pp. 197–203. ISSN: 1998-0124, 1998-0000. DOI: 10.1007/s12274-018-2202-x.

[32] A. M. Katzenmeyer et al. “Mid-Infrared Spectroscopy beyond the Diffraction Limit via Direct Measurement of the Photothermal Effect”. In: *Nanoscale* 7.42 (2015), pp. 17637–17641. ISSN: 2040-3364, 2040-3372. DOI: 10.1039/C5NR04854K.

[33] Alexandre Dazzi and Craig B. Prater. “AFM-IR: Technology and Applications in Nanoscale Infrared Spectroscopy and Chemical Imaging”. In: *Chemical Reviews* 117.7 (Apr. 12, 2017), pp. 5146–5173. ISSN: 0009-2665, 1520-6890. DOI: 10.1021/acs.chemrev.6b00448.

[34] Alexandre Dazzi et al. “AFM–IR: Combining Atomic Force Microscopy and Infrared Spectroscopy for Nanoscale Chemical Characterization”. In: *Applied Spectroscopy* 66.12 (2012), pp. 1365–1384. DOI: 10.1366/12-06804. pmid: 23231899.

[35] A. Catarina V. D. dos Santos et al. “Nanoscale Chemical Characterization of a Post-Consumer Recycled Polyolefin Blend Using Tapping Mode AFM-IR”. In: *The Analyst* (2022), 10.1039.D2AN00823H. ISSN: 0003-2654, 1364-5528. DOI: 10.1039/D2AN00823H.

Die approbierte gedruckte Originalversion dieser Diplomarbeit ist an der TU Wien Bibliothek verfügbar
The approved original version of this thesis is available in print at TU Wien Bibliothek.
TU Bibliothek Your knowledge hub WIEN

[36] Curtis Marcott et al. "Spatial Differentiation of Sub-Micrometer Domains in a Poly(Hydroxyalkanoate) Copolymer Using Instrumentation That Combines Atomic Force Microscopy (AFM) and Infrared (IR) Spectroscopy". In: *Appl. Spectrosc.* 65.10 (Oct. 2011), pp. 1145–1150. URL: http://opg.optica.org/as/abstract.cfm?URI=as-65-10-1145.

[37] L Baldassarre et al. "Mapping the Amide I Absorption in Single Bacteria and Mammalian Cells with Resonant Infrared Nanospectroscopy". In: *Nanotechnology* 27.7 (Feb. 19, 2016), p. 075101. ISSN: 0957-4484, 1361-6528. DOI: 10.1088/0957-4484/27/7/075101.

[38] A. Dazzi et al. "Chemical Mapping of the Distribution of Viruses into Infected Bacteria with a Photothermal Method". In: *Ultramicroscopy* 108.7 (June 2008), pp. 635–641. ISSN: 03043991. DOI: 10.1016/j.ultramic.2007.10.008.

[39] Michael K. F. Lo et al. "Nanoscale Chemical-Mechanical Characterization of Nanoelectronic Low- k Dielectric/Cu Interconnects". In: *ECS Journal of Solid State Science and Technology* 5.4 (2016), P3018–P3024. ISSN: 2162-8769, 2162-8777. DOI: 10.1149/2.0041604jss.

[40] Gerhard J. Schütz et al. "Protein Micropatterning Assay: Quantitative Analysis of Protein–Protein Interactions". In: *Proteomics*. Ed. by Lucio Comai, Jonathan E. Katz, and Parag Mallick. Vol. 1550. Methods in Molecular Biology. New York, NY: Springer New York, 2017, pp. 261–270. ISBN: 978-1-4939-6745-2 978-1-4939-6747-6. DOI: 10.1007/978-1-4939-6747-6_18.

[41] Marco Lindner et al. "A Fast and Simple Contact Printing Approach to Generate 2D Protein Nanopatterns". In: *Frontiers in Chemistry* 6 (Jan. 24, 2019), p. 655. ISSN: 2296-2646. DOI: 10.3389/fchem.2018.00655.

Die approbierte gedruckte Originalversion dieser Diplomarbeit ist an der TU Wien Bibliothek verfügbar
The approved original version of this thesis is available in print at TU Wien Bibliothek.
TU Bibliothek Your knowledge hub WIEN

[42] Shi Qiu et al. “Recent Advances in Surface Manipulation Using Micro-Contact Printing for Biomedical Applications”. In: *Smart Materials in Medicine* 2 (2021), pp. 65–73. ISSN: 25901834. DOI: 10.1016/j.smaim.2020.12.002.

[43] Izumi Kumagai and Kouhei Tsumoto. “Antigen–antibody binding”. In: *e LS* (2001).

[44] Iago Pereiro, Anna Fomitcheva-Khartchenko, and Govind V Kaigala. “Shake It or Shrink It: Mass Transport and Kinetics in Surface Bioassays Using Agitation and Microfluidics”. In: (), p. 18.

[45] Huey Wen Ooi et al. “Coordination Complexes as Molecular Glue for Immobilization of Antibodies on Cyclic Olefin Copolymer Surfaces”. In: *Analytical Biochemistry* 456 (July 2014), pp. 6–13. ISSN: 00032697. DOI: 10.1016/j.ab.2014.03.023.

[46] Ben W. Muir et al. “High-Throughput Optimization of Surfaces for Antibody Immobilization Using Metal Complexes”. In: *Analytical Biochemistry* 363.1 (Apr. 2007), pp. 97–107. ISSN: 00032697. DOI: 10.1016/j.ab.2007.01.015.

[47] J. V. Sengers and B. Kamgar-Parsi. “Representative Equations for the Viscosity of Water Substance”. In: *Journal of Physical and Chemical Reference Data* 13.1 (Jan. 1984), pp. 185–205. ISSN: 0047-2689, 1529-7845. DOI: 10.1063/1.555708.

[48] Mladenka Malenica et al. “Perspectives of Microscopy Methods for Morphology Characterisation of Extracellular Vesicles from Human Biofluids”. In: *Biomedicines* 9.6 (June 2021), p. 603. DOI: 10.3390/biomedicines9060603.

[49] Dirk-Jan Kroon. “NUMERICAL OPTIMIZATION OF KERNEL BASED IMAGE DERIVATIVES”. In: (2009).

[50] Laurent Najman and Michel Schmitt. “Watershed of a Continuous Function”. In: *Signal Processing* 38.1 (July 1994), pp. 99–112. ISSN: 01651684. DOI: 10.1016/0165-1684(94)90059-0.

Die approbierte gedruckte Originalversion dieser Diplomarbeit ist an der TU Wien Bibliothek verfügbar
The approved original version of this thesis is available in print at TU Wien Bibliothek.
TU Bibliothek Your knowledge hub WIEN

[51] Manuel Guizar-Sicairos, Samuel T. Thurman, and James R. Fienup. "Efficient Subpixel Image Registration Algorithms". In: *Opt. Lett.* 33.2 (Jan. 2008), pp. 156–158. DOI: 10.1364/OL.33.000156.

[52] Rabinarayan Satpathy et al., eds. *Data Analytics in Bioinformatics: A Machine Learning Perspective*. First edition. Hoboken, NJ: Wiley-Scrivener, 2021. 1 p. ISBN: 978-1-119-78560-6 978-1-119-78561-3.

[53] *1.2. Linear and Quadratic Discriminant Analysis*. scikit-learn. URL: https://scikit-learn/stable/modules/lda_qda.html (visited on 08/26/2022).

[54] Karl Pearson F.R.S. "LIII. On Lines and Planes of Closest Fit to Systems of Points in Space". In: *The London, Edinburgh, and Dublin Philosophical Magazine and Journal of Science* 2.11 (1901), pp. 559–572. DOI: 10.1080/14786440109462720.

[55] Hervé Abdi and Lynne J. Williams. "Principal Component Analysis". In: *WIREs Computational Statistics* 2.4 (2010), pp. 433–459. DOI: 10.1002/wics.101.

[56] *Probability Calibration Curves*. scikit-learn. URL: https://scikit-learn/stable/auto_examples/calibration/plot_calibration_curve.html (visited on 08/25/2022).

[57] Zanyar Movasaghi, Shazza Rehman, and Dr. Ihtesham ur Rehman. "Fourier Transform Infrared (FTIR) Spectroscopy of Biological Tissues". In: *Applied Spectroscopy Reviews* 43.2 (Feb. 2008), pp. 134–179. ISSN: 0570-4928, 1520-569X. DOI: 10.1080/05704920701829043.

[58] G. Socrates and G. Socrates. *Infrared and Raman Characteristic Group Frequencies: Tables and Charts*. 3rd ed. Chichester ; New York: Wiley, 2001. 347 pp. ISBN: 978-0-471-85298-8.

[59] Yu-Shiu Lo et al. "Organic and Inorganic Contamination on Commercial AFM Cantilevers". In: *Langmuir* 15.19 (Sept. 1, 1999), pp. 6522–6526. ISSN: 0743-7463, 1520-5827. DOI: 10.1021/la990371x.

Die approbierte gedruckte Originalversion dieser Diplomarbeit ist an der TU Wien Bibliothek verfügbar
The approved original version of this thesis is available in print at TU Wien Bibliothek.
TU Bibliothek Your knowledge hub WIEN

[60] Joseph A. Cottam, Andrew Lumsdaine, and Peter Wang. "Abstract Rendering: Out-of-Core Rendering for Information Visualization". In: IS&T/SPIE Electronic Imaging. Ed. by Pak Chung Wong et al. San Francisco, California, USA, Dec. 23, 2013, 90170K. DOI: 10.1117/12.2041200.

Die approbierte gedruckte Originalversion dieser Diplomarbeit ist an der TU Wien Bibliothek verfügbar
The approved original version of this thesis is available in print at TU Wien Bibliothek.
TU Bibliothek Your knowledge hub WIEN